# Analytical representation for amplitudes and differential cross section of pp elastic scattering at 13 TeV[*]

E. Ferreira[a], A. K. Kohara[b], and T. Kodama[a, c]

[a] Instituto de Física, Universidade Federal do Rio de Janeiro
C.P. 68528, Rio de Janeiro 21945-970, RJ, Brazil

[b] *Departamento de Engenharia Química,*
*Centro de Tecnologia da Indústria Química e Têxtil,*
*SENAI, Rio de Janeiro 20961-020, RJ, Brazil*

[c] *Instituto de Física, Universidade Federal Fluminense,*
*Niterói 24210-346, RJ, Brazil*

With analytical representation for the pp scattering amplitudes introduced and tested at lower energies, a description of high precision is given of the $d\sigma/dt$ data at $\sqrt{s}=$ 13 TeV for all values of the momentum transfer, with explicit identification of the real and imaginary parts. In both $t$ and $b$ coordinates the amplitudes have terms identified as of non-perturbative and perturbative nature, with distinction of their influences in forward and large $|t|$ ranges and in central and peripheral regions respectively. In the large $|t|$ extreme, the connection with the perturbative three-gluon exchange is claimed as characteristic universal (energy-independent) behavior and as explanation of the behaviour of the 13 TeV data beyond $|t| = 0.2$ GeV$^2$. In the forward range, the role of the Coulomb-nuclear interference phase is investigated.

## I. INTRODUCTION

Totem Collaboration in LHC has produced two sets of data data on elastic pp scattering at $\sqrt{s}=$13 TeV in separate publications [1–3], covering the following $|t|$ ranges

- Set I - $|t| = [0.000879 - 0.201041]$ GeV$^2$ , with N=138 points [1] ;

- Set II - $|t| = [0.0384 - 3.82873]$ GeV$^2$ , with N=290 points [2] .

With respect to systematic errors, the two sets of measurement are presented with very different features: errors of about 5% for I and less than 1% (except for the first 11 points) for Set II. The situation, illustrated in Fig.1, influences the analysis of the data. The very large large systematic errors in Set I indicates the necessity of special care on its use for the determination of the forward scattering structure.

There are 56 points of small $|t|$ in Set I, up to $|t| = 0.037335$ GeV$^2$, where Set II starts, and thus there is a basis of 56 + 290 = 346 data points to perform a global description of the 13 TeV data. We also build a combined file merging the points of the common range, with a total of 138+290=428 points that are used in an overall test.

The data of Set I have been studied [4] with forms of amplitudes restricted to small $|t|$ values. The treatment of this range requires detailed account of the Coulomb-nuclear interference, and it was shown that the model-independent determination of the amplitude in these representations is unreliable with the present data alone, due

to the small value of the $\rho$ parameter and to the assumption of a model for the treatment of the Coulomb-nuclear interference phase that needs to be tested at such high energies. In the forward direction the real part contributes to only about 1% of the observed $d\sigma/dt$, and it is necessary to have a well-inspired extraction of the imaginary part, requiring data of very regular behaviour, to allow the determination of the properties of the real part, such as the $\rho$ parameter and the amplitude slope.
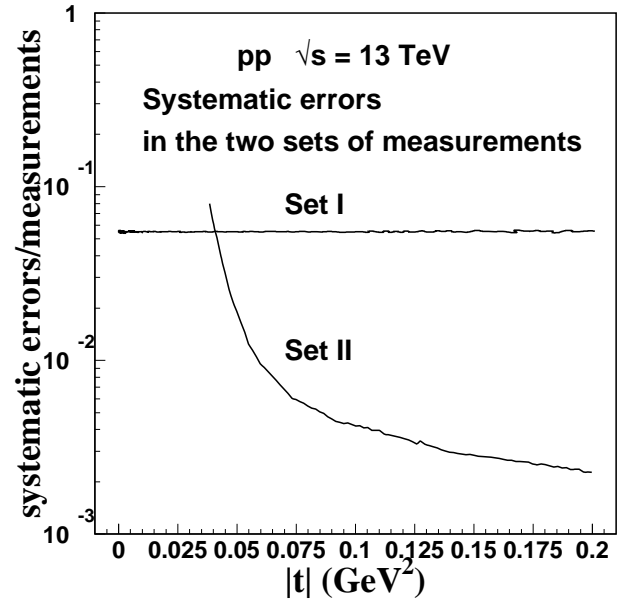


FIG. 1. Systematic errors in data Set I [1] and Set II [2]. In the $|t|$ range with superposition ($0.038400 \leq |t| \leq 0.201041$) it seems that in general the data in Set II may be considered as more reliable (1% systematic errors), except for the first 11 points. Set I has 5% systematic error bars.

Putting all information together, we give a unified treatment of 428 data points, identifying analytically the real and imaginary parts (with 4 parameters each) of the complex elastic amplitude, with remarkable values $\chi^2 = 1.567$ with statistical and systematic errors added in quadrature and $\chi^2 = 5.186$ calculated with statistical errors only. Everywhere in the present text $\chi^2$ is a short for $\chi^2/d.o.f.$. The graphical representation of this result is shown in Fig.2. The present treatment is similar to previous work that was very effective at lower energies 1.8 - 1.96 TeV of Fermilab [5] and 7-8 TeV of LHC [6, 7].

The large $|t|$ range of Set II is coupled sensibly with the (energy independent) tail of perturbative three-gluon exchange observed at $\sqrt{s} = 27.4$ GeV [8], with 39 points in the range $5.5 \leq |t| \leq 14.2$ GeV$^2$. The first identification of the energy independence of the $d\sigma/dt$ behaviour for large $|t|$ in pp elastic scattering was made in the comparison of data at $\sqrt{s} = 19.6$ and 27.4 GeV [9]. The theoretical explanation for the $1/|t|^8$ behaviour of $d\sigma/dt$ for large $|t|$ in terms of the real three-gluon exchange amplitude was given by Donnachie and Landshoff [10]. The universality is demonstrated for energies below $\sqrt{s} = 62.5$ GeV in Fermilab and CERN/ISR measurements [11, 12] (see figures in these two papers), showing smooth connection between the range of small and mid-$|t|$ combining perturbative and nonperturbative terms and the range of large $|t|$ of FNAL [8] measurements dominated by three-gluon exchange. The role of the real amplitude in the large $|t|$ sector of pp elastic scattering is then confirmed.

The transition range from 2 to 5 GeV$^2$ gives information on the magnitude and sign of the real part of the hadronic amplitude, that is dominant for large $|t|$. Unfortunately the LHC pp measurements at 7 and 8 TeV [6, 7] are restricted to $|t|$ less than 2 GeV$^2$, and the connection between mid and large $|t|$ regions remained in the non-quantitative level, although there is clear indication , as shown in Fig.6 of the 7 TeV paper [6], where the data at 52.8 GeV and 7 TeV are exhibited. At 13 TeV the measurements reach almost $|t| = 4$ GeV$^2$, allowing investigation in an important extended range. Using the same representation described above, with a proper connection between the 13 TeV and the 17.4 GeV data, we obtain an analytical form embracing 467 (= 428+39) data points, with $\chi^2 = 1.731$ and $\chi^2 = 5.042$ using total errors (combined statistical and systematic) and pure statistical errors respectively.

The present work uses the amplitudes introduced in previous papers [5–7], expressed in both $t$ and $b$ coordinates, with explicit forms for the real and imaginary amplitudes: the disentanglement of the two parts is essential for the description of the dynamics of the process. The superposition of non-perturbative and perturbative terms in both real and imaginary parts produces remarkable structure in the elastic differential cross section that faithfully reproduces the data. In the following this framework is referred to as KFK model.

In Sec.II we review the construction of the amplitudes

in the KFK model, inspired on the early applications of the Stochastic Vacuum Model (SVM) to high-energy elastic scattering. The $b$ and $t$ space coordinates are analytically related, with terms representing perturbative and non-perturbative dynamics.

In Sec.III we apply the KFK amplitudes to describe in detail the forward, mid and large $|t|$ ranges, obtaining a unique solution valid with high precision for all $|t|$, as shown in Fig.2. Separate attention is given to an extension of the representation to the range of high $|t|$ measured at 27.4 GeV [8] and also to the small $|t|$ range of Set I re-examining the role of the Coulomb-nuclear interference phase [4]. In Sec.IV, the properties of the amplitudes in $|t|$- and $b$- coordinates are described and discussed in separate subsections. Sec.V compares our description with other models and Sec.VI presents remarks and critical evaluation.

## II. KFK MODEL : ANALYTICAL REPRESENTATION OF THE AMPLITUDES

The KFK model writes analytical forms for the pp and p$\bar{\text{p}}$ elastic scattering amplitudes in $t$ and $b$ spaces. The model is based on previous experience with the Stochastic Vacuum Model (SVM) [13], using the loop-loop correlation length and the asymptotic (large $b$) behaviour of the profile function as ingredients. SVM is based on the functional integral approach to high energy scattering [14–16] that relates high energy scattering with
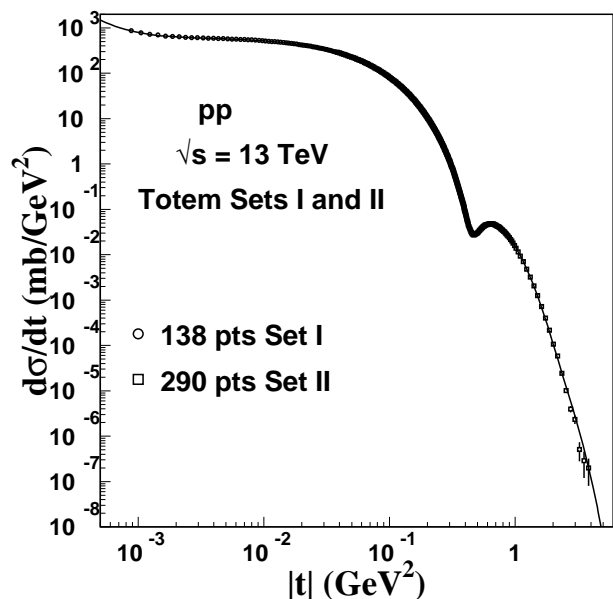


FIG. 2. Analytical representation of all data points of Totem measurements at 13 TeV [1, 2], using 4 adjusted parameters [5–7, 11] for each of the real and imaginary parts. The total of 428 data points is described with $\chi^2 = 1.567$ (statistical and systematic errors added in quadrature) and $\chi^2 = 5.186$ (statistical errors only). Details are given in Secs.II and III.

nontrivial properties of QCD vacuum. Non-perturbative hadron-hadron scattering is described in terms of correlation of Wilson loops [13, 17, 18] in the transverse collision plane. Using the non-commutative Stokes theorem and assuming dominance of Gaussian fluctuations in the field strengths, the calculation becomes fully analytical. Observables are written in terms of physical quantities: the value of the gluon condensate (that determines the strength of this non-perturbative dynamics) and the correlation length (parameter of the non-local loop-loop correlation function that sets the scale for the geometric dependence in $b$-space). These quantities have values fixed by hadronic properties and by lattice calculations [19]. Specific hadrons enter through their wave functions and a unified treatment of forward scattering is obtained for different hadronic pairs [13, 17, 18]. Energy dependence enters through the evolution of the hadronic sizes of the participating hadronic structures. Besides hadron-hadron scattering, the concept of the loop-loop correlation was also applied to the non-perturbative processes of photo- and electroproduction of vector mesons [18, 20, 21].

Later developments of SVM brought important progress [22], with new forms for correlation functions, suggested by extensive lattice calculations [23], and also a new term of perturbative nature was added to the dynamics. These quantities are part of the KFK model.

However, the original SVM calculation and further developments deal only with the imaginary part of the complex elastic amplitude, and cannot describe the differential cross section in the full $|t|$ range of the experiments. In the region of very small $|t|$ the real part is very small (about $1/10$ of the imaginary amplitude), and the original SVM is meaningful for the prediction of total cross sections and slopes. The real part is dominant for large $|t|$, and has crucial role in the dip-bump region of pp elastic scattering around 0.4-0.5 GeV$^2$ where the imaginary part passes through zero. The sophisticated dip-bump structure in $d\sigma/dt$ requires a proposal for the real part valid in this range. Both parts must have perturbative and non-perturbative terms, and must have zeros, signs and magnitudes following theoretical principles and reproducing observations [11, 12]. For example, it is known that, according to a theorem by A. Martin [24], the real part of the hadronic amplitude has a zero at small $|t|$, while the imaginary part has a zero responsible for the dip-bump structure in $d\sigma/dt$.

The analytical forms proposed for the non-perturbative terms of the amplitudes are inspired in the behaviour of the profile function for large $b$ found in the calculation with SVM [11, 13], with a combined exponential-Yukawa dependence. The Fourier transforms to $t$-space present features that can effectively represent the data for all $|t|$. The amplitudes must contain terms of perturbative and non-perturbative nature, as has also been introduced for the imaginary part in the more recent developments of SVM [18, 22]. As $b$ is not an observable quantity, the detailed construction is tested in $|t|$ space, and parameters are fixed by experiments. Accurate description of the data is obtained with four parameters in each part of the complex amplitude [11].

The disentanglement of the two parts of the complex amplitude is not at all trivial. The connection with the three-gluon exchange contribution helps in the identification of the sign and magnitude of the real part, and an additional term for perturbative three-gluon exchange of the FNAL measurements [8] is introduced separately. The KFK model has been investigated at several energies, and the energy dependence of the parameters comes out smooth, with simple parametrization [5–7].

## A. Impact parameter representation

The amplitudes in the Stochastic Vacuum Model [13] are originally constructed through $b$-space profile functions, that give insight for geometric aspects of the collision, playing role in the eikonal representation, where unitarity constraints have interesting formulation. The dimensionless $(s, b)$ amplitudes of the pure nuclear interaction are written in the form

$$\widetilde{T}_K(s, \vec{b}) = \frac{\alpha_K}{2\beta_K} e^{-b^2/4\beta_K} + \lambda_K \widetilde{\psi}_K(s, b) , \qquad (1)$$

with a Gaussian term meant to be of perturbative nature and a characteristic non-perturbative shape function

$$\widetilde{\psi}_K(s, b) = \frac{2e^{\gamma_K - \sqrt{\gamma_K^2 + b^2/a^2}}}{a^2\sqrt{\gamma_K^2 + b^2/a^2}} \left[1 - e^{\gamma_K - \sqrt{\gamma_K^2 + b^2/a^2}}\right] . \quad (2)$$

The label $K = R, I$ indicates either the real or the imaginary part of the complex amplitude. The quantity $a$, called correlation length, represents properties of the QCD vacuum and sets the scale for the loop-loop correlation. It is estimated in lattice calculations [19] with an accuracy of about 20 percent, and is used here with central value

$$a^2 = 2.1468 \pm 0.0001 \ \text{GeV}^{-2} = (0.2891 \pm 0.0002 \ \text{fm})^2. \quad (3)$$

The parameters $\alpha_K(s), \beta_K(s), \lambda_K(s)$ with units in GeV$^{-2}$ and $\gamma_K(s)$ dimensionless are functions of the energy. They are determined for $\sqrt{(s)} = 13$ TeV with high precision in Sec.III, leading to explicit analytical expressions for the imaginary and real amplitudes. The Gaussian form of the first term in Eq.(1) corresponds to the perturbative part of the loop-loop correlation introduced in developments of SVM, following results suggested by lattice calculations. The second term, referred to as shape function, corresponds to contributions from non-perturbative loop-loop correlation function. It is zero at $b = 0$, $\widetilde{\psi}_K(s, b = 0) = 0$, and is normalized as

$$\frac{1}{2\pi} \int d^2\vec{b} \ \tilde{\psi}_K(b, s) = 1 . \qquad (4)$$

Eq.(1) represents a parametrized formulation of the profile function based on the SVM proposal. The perturbative and non-perturbative terms of the amplitudes are dominant for small and large $b$ respectively. For large $b$, corresponding to peripheral collisions, the amplitudes fall down with a exponential-Yukawa-like tail,

$$\sim \frac{1}{b} e^{-b/b_0}, \tag{5}$$

that reflects the correlations of loops at large distances. This asymptotic behaviour inspired the construction of the shape function $\widetilde{\psi}_K(s,b)$ for Eq.(1).

## B.    $t$-space representation

In the classical limit the variable $b$ is connected with the impact parameter, but it is not directly observable, and the treatment of data is made in $(s,t)$ space. One advantage of the shape function in KFK is that there is explicit analytic Fourier transformation for the amplitudes in Eqs.(1,2), so that the scattering properties can be studied directly in both frameworks.

In our normalization the elastic differential cross section is written

$$\frac{d\sigma(s,t)}{dt} = (\hbar c)^2 [T_I^2(s,t) + T_R^2(s,t)] \tag{6}$$
$$= \frac{d\sigma^I(s,t)}{dt} + \frac{d\sigma^R(s,t)}{dt} ,$$

with $T_R(s,t)$ and $T_I(s,t)$ in $\text{GeV}^{-2}$ units, and

$$(\hbar c)^2 = 0.389379 \, \text{mb}\,\text{GeV}^2 .$$

The complete amplitudes , contain the nuclear and the Coulomb parts as

$$T_R(s,t) = T_R^N(s,t) + \sqrt{\pi} F^C(t) \cos(\alpha\Phi) , \tag{7}$$

and

$$T_I(s,t) = T_I^N(s,t) + \sqrt{\pi} F^C(t) \sin(\alpha\Phi) , \tag{8}$$

where $\alpha$ is the fine-structure constant, $\Phi(s,t)$ is the interference phase (CNI) and $F^C(t)$ is related with the proton form factor

$$F^C(t) = (-/+) \frac{2\alpha}{|t|} F_{\text{proton}}^2(t) , \tag{9}$$

for the pp/p$\bar{\text{p}}$ collisions. The proton form factor is taken as

$$F_{\text{proton}}(t) = [t_0/(t_0 + |t|)]^2 , \tag{10}$$

where $t_0 = 0.71 \, \text{GeV}^2$.

We recall the new measurements of the proton radius [25] and changes in the proton form factor [26]. These changes in the electromagnetic and hadronic structure

of the proton may become important for the analysis of forward elastic scattering, when their quality improves. As it has been proved [4], this is not the case at the present, and we use the quantities as written above.

The expressions $T_R^N(s,t)$ and $T_I^N(s,t)$ represent the nuclear amplitudes for the terms written in Eq.(1). The non-perturbative shape functions in $t$-space obtained by Fourier transforms are written

$$\Psi_K(\gamma_K(s),t) \tag{11}$$
$$= 2 \, e^{\gamma_K} \left[ \frac{e^{-\gamma_K\sqrt{1+a^2|t|}}}{\sqrt{1+a^2|t|}} - e^{\gamma_K} \frac{e^{-\gamma_K\sqrt{4+a^2|t|}}}{\sqrt{4+a^2|t|}} \right] ,$$

with the property

$$\Psi_K(\gamma_K(s), t=0) = 1 . \tag{12}$$

Use is made of the integration formula

$$\int_0^\infty J_0(\beta u) \frac{e^{-\rho\sqrt{\gamma^2+u^2}}}{\sqrt{\gamma^2+u^2}} u \, du = \frac{e^{-\gamma\sqrt{\rho^2+\beta^2}}}{\sqrt{\rho^2+\beta^2}} . \tag{13}$$

In addition to the Fourier transform of the perturbative part in Eq.(1) we introduce in the real part a term $R_{ggg}(t)$ representing the perturbative three-gluon exchange [10, 11] that appears in the large $|t|$ region, and the complete nuclear amplitudes are then written

$$T_K^N(s,t) \to T_K^N(s,t) \tag{14}$$
$$= \alpha_K(s) e^{-\beta_K(s)|t|} + \lambda_K(s) \Psi_K(\gamma_K(s), t)$$
$$+ \delta_{K,R} R_{ggg}(t), \quad K = R, I ,$$

with $K = R, I$, and where the Kronecker delta symbol $\delta_{K,R}$ is introduced so that $R_{ggg}(t)$ contributes only to the real part. Eqs.(11,14) constitute the KFK model for the pp and p$\bar{\text{p}}$ elastic amplitudes in $t$ space.

The limits of the amplitudes for small $|t|$ give the total cross section $\sigma$(optical theorem), the ratio $\rho$ of the real to imaginary amplitudes and the slopes $B_{R,I}$ at $t=0$ through

$$\sigma(s) = (\hbar c)^2 \, 4\sqrt{\pi} \, T_I^N(s, t=0) \tag{15}$$
$$= 4\sqrt{\pi} \, (\hbar c)^2 \, [\alpha_I(s) + \lambda_I(s)]$$
$$= 2.7606 \, [\alpha_I(s) + \lambda_I(s)] \, \text{mb} ,$$

$$\rho(s) = \frac{T_R^N(s, t=0)}{T_I^N(s, t=0)} = \frac{\alpha_R(s) + \lambda_R(s)}{\alpha_I(s) + \lambda_I(s)} \tag{16}$$

and

$$B_K(s) = \frac{2}{T_K^N(s,t)} \frac{dT_K^N(s,t)}{dt}\bigg|_{t=0} = \frac{1}{\alpha_K(s) + \lambda_K(s)} \times$$
$$\left[ \alpha_K(s)\beta_K(s) + \frac{1}{8}\lambda_K(s)a^2\Big(6\gamma_K(s) + 7\Big) \right] . \tag{17}$$

The tail term $R_{ggg}(t)$, producing a universal (not energy dependent) $|t|^{-8}$ form for large $|t|$ in $d\sigma/dt$ was studied in the analysis of the experiments at CERN-ISR,

CERN-SPS [11], 1.8 TeV [7] and 7 TeV [5]. To restrict this contribution to the large $|t|$ region, we create a connection factor, writing

$$R_{ggg}(t) \equiv \pm \frac{d_1}{t^4}[1 - e^{-d_2(t^2 - d_0)}][1 - e^{-\mathrm{x}t}]^{d_3} , \qquad (18)$$

where the last two factors cut-off this term smoothly in the domain from 2 to 5.5 GeV$^2$, and the signs $\pm$ refer to the pp and p$\bar{\mathrm{p}}$ amplitudes respectively. The detailed form of the factor in Eq.(18) must be adequate for the description of the data for $|t|$ values in the transition range connecting the experimental points [8] at $\sqrt{s} = 27.4\,\mathrm{GeV}$. In Sec.III, the proposed parameters are

$$d_0 = 9 \ \mathrm{GeV}^4, \ d_1 = 0.563 \pm 0.008\,\mathrm{GeV}^6 , \qquad (19)$$
$$d_2 = 0.16 \pm 0.01\,\mathrm{GeV}^{-4} , \ d_3 = 48 , \ \mathrm{x} = 1\,\mathrm{GeV}^{-2} .$$

The peculiar form of Eq.(18) is explained in Subsection III A.

## III. DESCRIPTION OF THE 13 TeV DATA

In this section we obtain the representation of the data of Totem experiment at 13 TeV through the $t$-space amplitudes of the KFK model written in Eqs.(11,14,18). Plots in Fig.3 show separately forward, mid and full $|t|$ ranges of the data of Sets I and II, described by a unique solution, with the parameters given in Table I. Table II gives statistical quantities for different ranges of the data, obtained with the same unique solution. Values of $\chi^2$ (in this paper we write $\chi^2$ as a short for $\chi^2/d.o.f.$) are given for calculations with statistical errors and for total errors combining statistical and systematic errors in quadrature. We also inform the $\chi^2$ value for a combined set of the first 56 points of Set I with the 290 points of Set II (total 346 points), avoiding the superposition of ranges. In the last line of Table II we inform the $\chi^2$ result for a set of 467 points joining the 27.4 GeV data [8], using the real amplitude that includes the $R_{ggg}$ term of 3-gluon exchange as in Eqs.(14, 18), while keeping fixed the parameters of Table I. The connection of the data of these different energies is illustrated in Subsec.III A. In Subsec.III B we present specific results of an analysis for the forward data of Set I.

Some quantities derived from the unique solution are given in Table III.

### A. Connection with measurements at $\sqrt{s} = 27.4\,\mathrm{GeV}$

The elastic scattering data for $|t|$ larger than 5 GeV$^2$ have been shown to be independent of the energy in a large range of $\sqrt{s}$ from 20 GeV to 7 TeV [5, 8, 9, 11]. The experiment at $\sqrt{s} = 27.4\,\mathrm{GeV}$ with 39 data points covering the wide $|t|$ range from 5.5 to 14.2 GeV$^2$ [8], provides important reference for the study of pp at large

scattering angles. The property is demonstrated for energies below $\sqrt{s} = 62.5$ GeV in Fermilab and CERN/ISR measurements [11] (see Figures 2,3 and 10 in this paper), showing a smooth connection between the mid-$|t|$ range containing perturbative and nonperturbative terms and the range of large $|t|$ dominated by perturbative three-gluon exchange.

The universality in the energy and the $|t|$ dependence of form $1/|t|^8$ in $d\sigma/dt$ have been interpreted by Donnachie and Landshoff [10] as determined by the process of exchange of three gluons. This contribution is represented by the quantity $R_{ggg}(|t|)$ introduced in Eq.(14), receiving a cut-off factor written in Eq.(18) designed to restrict the $1/|t|^8$ behaviour. The three-gluon contribution occurs in the $|t|$ range where the imaginary part is negligible, and the perturbative term $\alpha_R \ \exp(-\beta_R |t|)$ is dominant. The transition from 2 to 5 GeV$^2$ is precious to inform features (signs, magnitudes) of terms of the real scattering amplitude in the large $|t|$ region. These features are described in Sec.IV.

As an example, the structure of the real amplitude leads to the argument that the difference in the dip regions of pp and p$\bar{\mathrm{p}}$ scattering at 53 GeV [27] is due to the difference in the signs of the three-gluon contributions in pp and p$\bar{\mathrm{p}}$ scattering, and not necessarily to the presence of an odderon element [11], unless it is meant that three-gluon exchange is the modern QCD name for odderon [28, 29].

At high energies, there is not sufficient experimental information for the investigation of the elastic amplitudes at high $|t|$. LHC measurements at 7 and 8 TeV [6, 7] are restricted to less than $|t| = 2$ GeV$^2$, and the connection between mid and large $|t|$ regions remains in the level of *clear indication*, as shown in Fig.6 of the 7 TeV paper [6], where the data for 52.8 GeV [30, 31] and 7 TeV are exhibited together.

At 13 TeV the data are a little more extended in $|t|$, reaching nearly 4 GeV$^2$, allowing investigation of properties of the amplitudes in the connection with FNAL data [8]. Then we first choose the parameters for the $R_{ggg}(t)$ function, that is shown Fig.4, together with the corresponding cross section in the range of the transition. In Fig.5 we show the matching of the Totem 13 TeV and ISR 52.806 GeV measurements [30, 31] with the data of FNAL measurements [8] at $\sqrt{s} = 27.4\,\mathrm{GeV}$.

Some points of high $|t|$ of the Totem measurements show a marked decrease in the values of $d\sigma/dt$, with large statistical error bars, from 45% to 60%. These points deviate meaningfully from the proposed solution, and particularly they seem not to accept easily the suggestion of connectivity with the three-gluon tail. These are only few points of poor statistics, but visually they have important influence, as shown in Figs.4 and 5. In our description, this range of $d\sigma/dt$ is dominated by the perturbative term in the real amplitude, and serves as important test of the proposed disentanglement. In Sec.IV we show that the real part of the KFK amplitude is positive for large $|t|$, and then the superposition with the

TABLE I. Parameters of the amplitudes in the KFK model determined with the 428 points of Totem measurements at 13 TeV. The QCD quantity related to correlation function is $a^2 = 2.1468 \pm 0.0001$ GeV$^{-2}$ = $(1.4652$ GeV$^{-1} \pm 0.0002)^2$ = $(0.2891 \pm 0.0002$ fm$)^2$ , where $a$ is called correlation length. The quantities $\gamma_I$ and $\gamma_R$ characteristic of the non-perturbative shape functions in Eq.(11) are dimensionless, while $\alpha_K$, $\beta_K$ and $\lambda_K$ have units GeV$^{-2}$. The index $K$ means $I, R$.

| Imaginary Amplitude | | | | Real Amplitude | | | |
|---|---|---|---|---|---|---|---|
| $\alpha_I$ GeV$^{-2}$ | $\beta_I$ GeV$^{-2}$ | $\lambda_I$ GeV$^{-2}$ | $\gamma_I$ | $\alpha_R$ GeV$^{-2}$ | $\beta_R$ GeV$^{-2}$ | $\lambda_R$ GeV$^{-2}$ | $\gamma_R$ |
| $15.701 \pm 0.001$ | $4.323 \pm 0.001$ | $24.709 \pm 0.002$ | $7.819 \pm 0.0005$ | $0.2922 \pm 0.0005$ | $1.540 \pm 0.003$ | $4.472 \pm 0.003$ | $7.503 \pm 0.006$ |

TABLE II. $\chi^2$ (namely $\chi^2/d.o.f.$) values for several ranges of the 13 TeV data, with the analytical forms of the KFK model given by Eqs.(11,14,18). The *unique solution* given in Table I is used in the determination of $\chi^2$ for all selected ranges shown in this table and in the plots of Fig.3. " With tail" means that extra 3-gluon exchange perturbative contribution of Eq.(18) is added to the analytical basis. In the calculations of this table the CNI (Coulomb-nuclear interference) phase is put equal to zero. Values of $\chi^2$ calculated with statistical errors only and with total errors formed by quadrature of statistical and systematic errors are shown. The 39 points of 27.4 GeV enter with statistical errors only.

| N pts | $\lvert t\rvert$ range GeV$^2$ | $\langle\chi^2\rangle$(total) no tail | $\langle\chi^2\rangle$(total) with tail | $\langle\chi^2\rangle$(stat) no tail | $\langle\chi^2\rangle$(stat) with tail | Remarks |
|---|---|---|---|---|---|---|
| 138 | 0.000879-0.201041 | 0.0162 | — | 1.455 | | entire Set I |
| 260 | 0.000879-0.24902 | 0.2737 | — | 4.852 | | Set I(138) + Forward Set II (122) |
| 122 | 0.0384-0.24902 | 0.5866 | — | 9.066 | | Forward part of Set II |
| 144 | 0.25643-0.89633 | 3.068 | — | 5.643 | | dip-bump region in Set II |
| 152 | 0.25643-1.15991 | 3.187 | — | 5.690 | | extended dip-bump region in Set II |
| 24 | 0.91528-3.82873 | 10.74 | 12.72 | 11.73 | 13.70 | range of highest $\lvert t\rvert$ in Set II |
| 290 | 0.0384-3.82873 | 2.326 | 2.448 | 7.052 | 7.164 | entire Set II |
| 346 | 0.000879-3.82873 | 1.943 | 2.044 | 6.142 | 6.235 | Set I(56) + Set II(290) |
| 428 | 0.000879-3.82873 | 1.567 | 1.642 | 5.186 | 5.260 | Set I(138) + Set II(290) |
| 385 | 0.000879-14.2 | — | 2.103 | — | 5.869 | Set I(56) + Set II(290) + Faissler et al (39) |
| 467 | 0.000879-14.2 | — | 1.731 | — | 5.042 | Set I(138) + Set II(290) + Faissler et al (39) |

also positive three-gluon term should be constructive. If the real part were negative, a dip could be formed. In the analysis of the 1.8/1.96 GeV Fermilab [5] p$\bar{\text{p}}$ data we predicted that such dip would appear for large $\lvert t\rvert$ (the three gluon term is negative in p$\bar{\text{p}}$ ), but unfortunately the measurements do not reach large enough $\lvert t\rvert$, and the prediction is not tested. Here in pp at 13 TeV, we do not have simple explanation for the decrease of $d\sigma/dt$ in the points of largest $\lvert t\rvert$. A connection function producing the visual shape would not be natural. This question obviously leads to the suggestion that the measurements in the large $\lvert t\rvert$ range should receive more attention.

Table II shows that the 24 points of with highest $\lvert t\rvert$ in Set II are described in our unique solution with comparatively large $\chi^2$ values of about 10. This is a local feature, as these points have low influence in the $\chi^2$ value for the 428 points. For a local investigation, we observe that this range is dominated by the perturbative real part, so that only the parameters $\alpha_R$ and $\beta_R$ require attention. Thus, with $\alpha_R = 0.476 \pm 0.022$ and $\beta_R = 1.771 \pm 0.025$ we obtain $\chi^2 = 2.210$ and $\chi^2 = 2.484$, respectively using total and only statistical errors. This predicted local improvement in $\chi^2$ changing only two selected parameters is consequence of the separation of the perturbative and non-perturbative terms in the analytical form.

**B. Specific representation of amplitudes for the 138 points of Set I**

As a side information (since the main concern of the present work is with the unique global solution for all ranges), in Table IV we show the $\chi^2$ results for the 138 points of Set I with freedom given to the $\lambda_I$ and $\lambda_R$ parameters, maintaining all other quantities as written and used in Tables I and II. Only the non-perturbative magnitudes $\lambda_I$ and $\lambda_R$ are investigated in this alternative examination because these terms are dominant in the imaginary and real amplitudes for small $\lvert t\rvert$, as shown in Sec.IV. Comparison is made of solutions with and without inclusion of the Coulomb-nuclear interference phase $\phi$. The results in Table IV may be compared with values obtained with simplified forms of amplitudes restricted to the forward scattering range [4], namely with product of exponential and linear factors as

$$T_K(t) = T_K(0) \, e^{(B_K^0/2)t}(1 - \mu_K \, t) \quad , K = I, R \ . \quad (20)$$

We again stress that the parameters $\sigma$, $\rho$ and slopes are model-dependent quantities, related to specific analytical forms of the amplitudes. The only experimental measurements are the values of $d\sigma/dt$ at angular positions defined by values of $\lvert t\rvert$. In particular, for the value of $\rho$, it has been shown [4] that the presently available data at small $\lvert t\rvert$ does not allow a conclusion about its value. Besides the insufficiency of regular data in the very forward

TABLE III. Quantities derived from the solution of the fitting of the 13 TeV data, with the parameters given in Table I. The quantities $Z_I$, $Z_R^{(1)}$ and $Z_R^{(2)}$ are the locations ($|t|$ values) of the zeros of the imaginary and real amplitudes. Properties of the amplitudes are discussed in Sec.IV.

| Imaginary Amplitude | | | | Real Amplitude | | | Elast. | Inel. | Dip | |
| --- | --- | --- | --- | --- | --- | --- | --- | --- | --- | --- |
| $\sigma$ | $Z_I$ | $B_I$ | $\rho$ | $Z_R^{(1)}$ | $Z_R^{(2)}$ | $B_R$ | $\sigma_{\rm el}$ | $\sigma_{\rm inel}$ | $|t|_{\rm dip}$ | $h_{\rm dip}$ |
| mb | $\mathrm{GeV}^2$ | $\mathrm{GeV}^{-2}$ | | $\mathrm{GeV}^2$ | $\mathrm{GeV}^2$ | $\mathrm{GeV}^{-2}$ | mb | mb | $\mathrm{GeV}^2$ | mb$/\mathrm{GeV}^2$ |
| $111.56 \pm 0.01$ | $0.46 \pm 0.01$ | $21.05 \pm 0.01$ | $0.118 \pm 0.001$ | $0.200 \pm 0.001$ | $1.180 \pm 0.010$ | $26.39 \pm 0.06$ | 31.10 | 80.46 | 0.47 | 0.025 |

region, the theoretical basis for the Coulomb-nuclear interference phase is uncertain.

We remark that both imaginary and real parts have zeros, so that, besides exponential slopes at least linear factors in the amplitudes are essential to represent the forward data realistically as in Eq.(20). In KFK the factorization of the logarithmic derivative with a slope as in Eq.(17) leaves a remainder that has a zero, but not a linear zero (actually the remaining factor has zero of higher order in a Taylor expansion), so that $B_I$ and $B_R$ in Eq.(17) correspond to the *effective* slope that includes the effect of a linear factor in the forward amplitude. The effective slope in Eq.(20) comparable to Eq.(17) is $B_K^{\rm eff} = B_K^0 - 2\mu_K$. It is also interesting to compare the value of the first real zero $Z_R^{(1)}$ of the KFK model in Table III with the values obtained [4] with Eq.(20). With $\mu_R = -3.84 \ \mathrm{GeV}^{-2}$, the zero at $|t| = -t = -1/\mu_R = 0.26 \, \mathrm{GeV}^2$ may be compared with $Z_R = 0.20 \, \mathrm{GeV}^2$ in Table III.
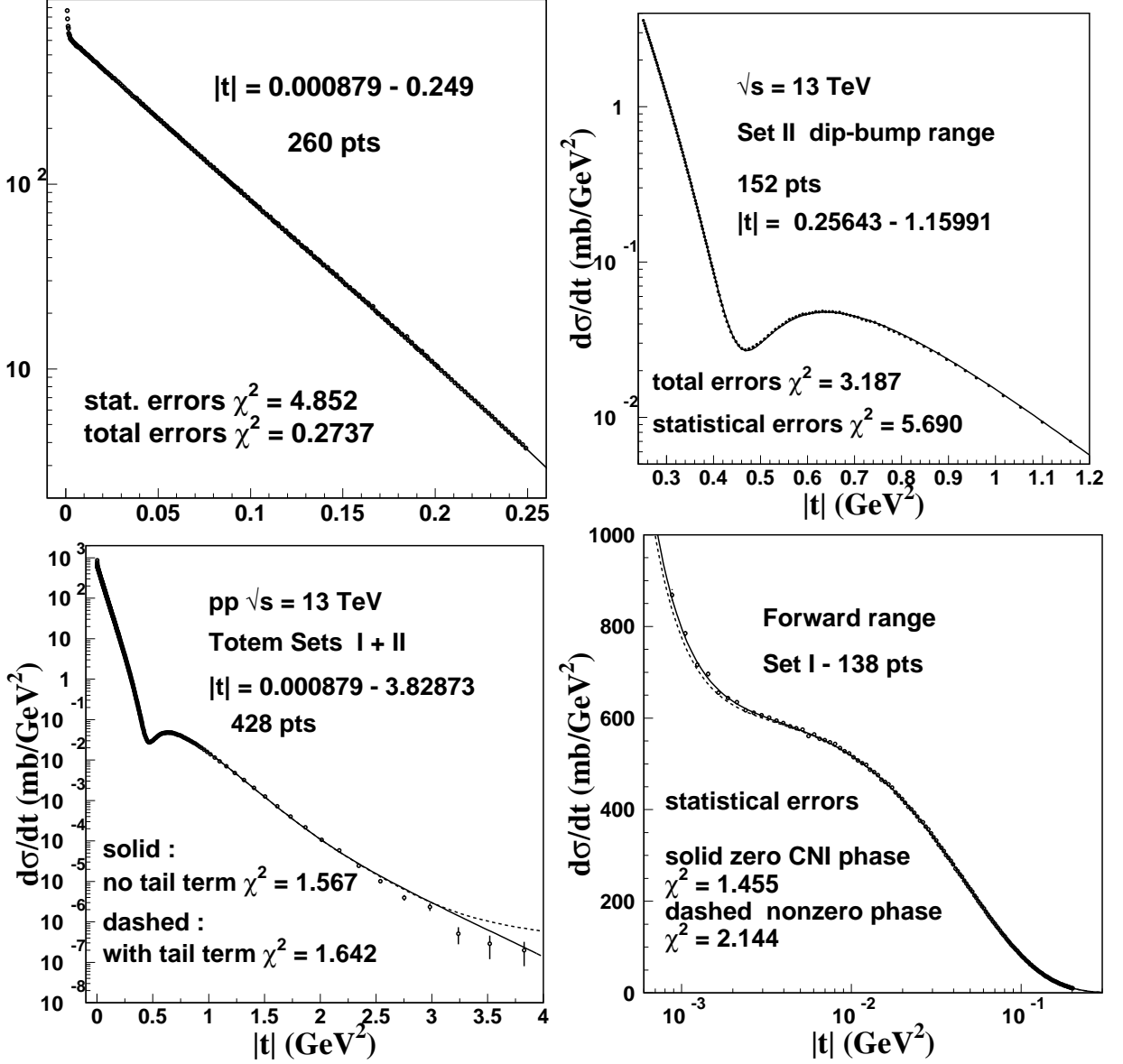
FIG. 3. Representation in the KFK model of separate $|t|$ ranges of Sets I and II of Totem measurements at 13 TeV, with unique analytical form and parameter values given in Table I. Plot c) shows in dashed line the displacement due to the inclusion of the $R_{ggg}(t)$ term in the amplitude. In Fig.5 we show how this term implies the connection with the data of large $|t|$ at $\sqrt{s} = 27.4\,\mathrm{GeV}$. In the small- and mid-$|t|$ ranges of plots a) and b) the influence of the tail term is not relevant in the plots. In plot d) for small $|t|$ we show lines for calculations with Coulomb-nuclear interference phase $\phi$ included in the usual form (dashed line), and with phase put as zero (solid line); numbers are given in Table IV.

TABLE IV. Values of parameters $\lambda_I$ and $\lambda_R$ and of $\chi^2$ (with statistical errors only) obtained specifically for the 138 points of Set I, with all other quantities ($\alpha_K$, $\beta_K$, $\gamma_K$) kept as given in Table I and used in Table II. We here give the values for fitting with Coulomb interference phase $\phi$ put as zero, and for phase calculated as described before [4]. The $\chi^2$ values may be compared with $\chi^2 = 1.455$ (with CNI phase zero) given in Table II and $\chi^2 = 2.144$ with CNI phase calculated with proton form factor. We recall that in the detailed analysis of forward data studying the influence of the CNI phase [4], reported values are $\sigma = 111.84$ mb, $\rho = 0.125$ for $\phi = 0$ , and $\sigma = 111.84$ mb, $\rho = 0.097$ for $\phi \neq 0$. The position $Z_R^{(1)}$ of the first real zero (Martin's Zero) is also given, since it occurs in the forward range and is important theoretical reference.

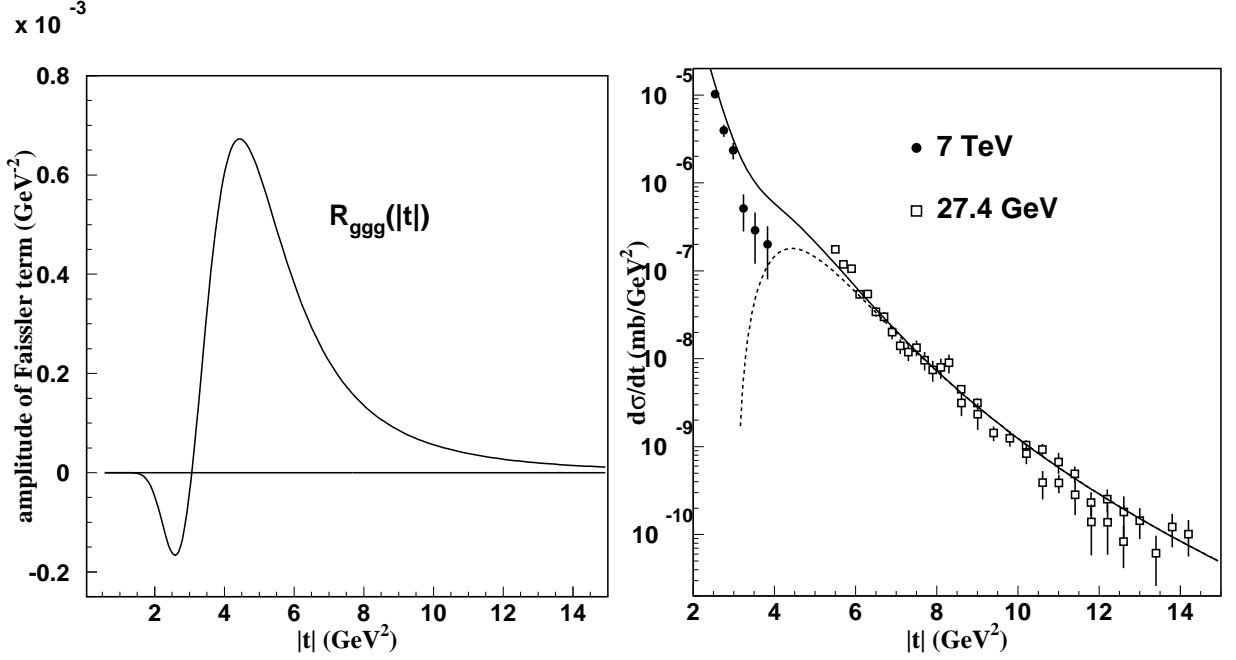| CNI phase $\phi$ | $\lambda_I$ GeV$^{-2}$ | $\lambda_R$ GeV$^{-2}$ | $\chi^2$ | $\sigma$ mb | $\rho$ | $B_I$ GeV$^{-2}$ | $B_R$ GeV$^{-2}$ | $Z_R^{(1)}$ GeV$^2$ |
|---|---|---|---|---|---|---|---|---|
| zero | $24.772 \pm 0.010$ | $4.382 \pm 0.115$ | 1.126 | $111.73 \pm 0.03$ | $0.116 \pm 0.001$ | 21.06 | 26.37 | 0.201 |
| $\phi(t)$ | $24.836 \pm 0.010$ | $3.403 \pm 0.130$ | 1.121 | $111.91 \pm 0.03$ | $0.092 \pm 0.001$ | 21.08 | 25.96 | 0.213 |

FIG. 4. Connection of the low energy ($\sqrt{s} = 27.4$ GeV) points of large $|t|$ ($5.5 \leq |t|| \leq 14.2$ GeV$^2$) with Totem 13 TeV data. a) Form proposed for the amplitude $R_{ggg}(|t|)$ in Eq.(18) for three-gluon exchange with a cut-off factor acting for $|t| \leq 4$ GeV$^2$. b) Differential cross section calculated including the $R_{ggg}(|t|)$ term (solid line) plotted together with points of Totem measurements at 13 TeV (full circles) and the points (open squares) at 27.4 GeV. The piece of dashed line pointing downwards shows the action of the cut-off factor.
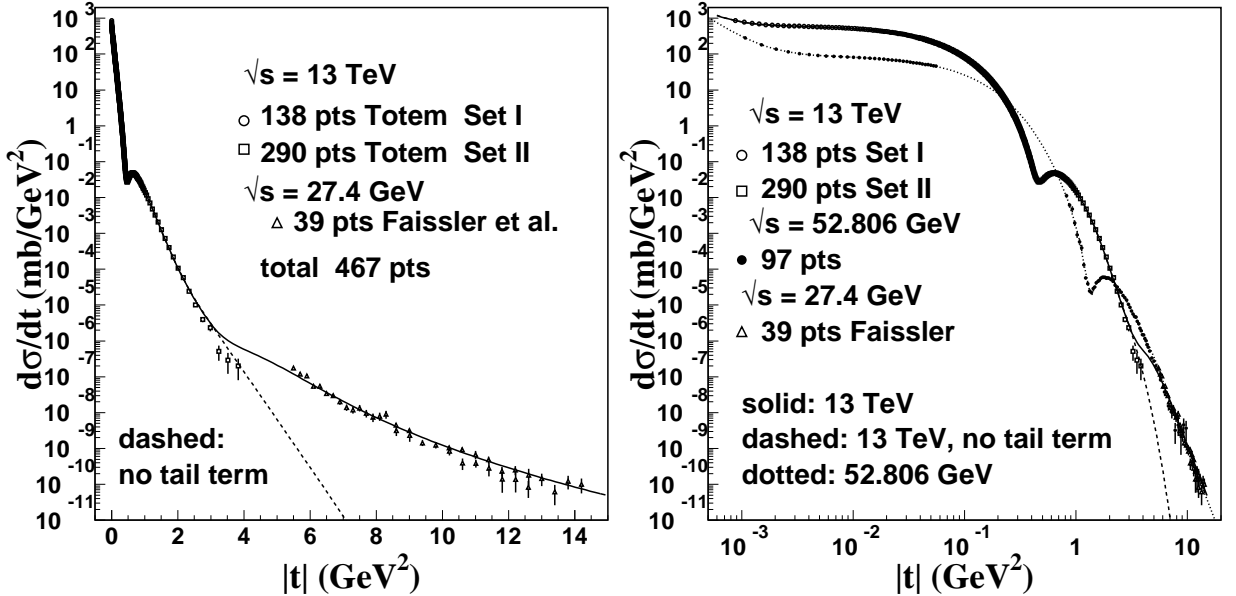


FIG. 5. a) Analytical representation for all 467 data points : 138 points of Set I [1] and 290 of Set II [2] from Totem measurements at 13 TeV, plus 39 points at $\sqrt{s} = 27.4$ GeV from FNAL measurements [8]. The global representation of 467 (138+290+39) points is constructed with the unique solution given in Table I plus the $R_{ggg}(t)$ term as in Eq.(14), with results $\chi^2 = 1.731$ (total statistical and systematic errors) and $\chi^2 = 5.042$ (statistical errors), as shown in Table II. The dashed lines represent the analytical form for 13 TeV excluding the 3-gluon exchange tail term. b) Joint plot of data at 52.806 GeV [30, 31] and Totem 13 TeV data, with the analytic solutions obtained with the KFK model [6]. The points have energy scales differing by more than 200, and still the data in the large $|t|$ region have similar magnitudes. The universality is consistently present at ISR energies [11, 12].

## IV. IMAGINARY AND REAL PARTS OF THE SCATTERING AMPLITUDE

The analysis presented in Sec.III leads to a proposal for the disentanglement of the real and imaginary parts, that is obtained directly from the data. In this section we discuss the properties of the amplitudes and their terms, in both $t$ and $b$ coordinates.

### A. Amplitudes in $t$ space

Fig.6 shows the amplitudes, detailing small and large $|t|$ ranges. Similarly to lower energies, the imaginary and real parts have one and two zeros respectively. In the plot for large $|t|$, the contribution of the the $R_{ggg}$ tail term is also shown, appearing as a deviation in the real amplitude visible for $|t| \geq 3\,\mathrm{GeV}^2$.

The separate perturbative and nonperturbative parts of the imaginary and real amplitudes are shown in Fig.7. The quantities. $T_I(\mathrm{pert}) = \alpha_I e^{-\beta_I|t|}$ and $T_I(\mathrm{nonpert}) = \lambda_I \Psi_I(\gamma_I, t)$ are strong and with opposite signs in the dip-bump region, with a cancellation at $Z_I = 0.46$ GeV$^2$, causing the dip. The existence of these two terms in $T_I$ is most important for the construction of the representation. The cancellation leaves room for the influence of the real amplitude that modulates the shape of the dip-bump structure. $T_R(\mathrm{nonpert})$ dominates (in magnitude) over $T_R(\mathrm{pert})$ in the dip-bump region, but if falls to zero more rapidly, while the perturbative real part lasts longer in $|t|$. For $|t|$ larger than $\sim 3$ GeV$^2$ only the perturbative real part $T_R(\mathrm{pert})(t)$ remains active, with positive sign.

As a general view, we observe that forward scattering emphasizes non-perturbative dynamics, while large $|t|$ scattering is dominated by perturbative terms in the real amplitude. The KFK parametrization in energy [7] says that $\lambda_I$ increases with $\log^2 s$, while $\alpha_I$ grows with $\log s$. Thus, forward scattering becomes more predominantly non-perturbative at high energies. The real part becomes negligible for $|t| = 0$, as $\rho$ decreases fast with the energy according to dispersion relations.

The magnitudes of all terms in the amplitudes vary enormously from the bump to the region $|t| = $ 3-4 GeV$^2$ reached by the present data. The structure in the large $|t|$ range that we try to access through the connection with the three-gluon exchange is important for the construction of a global picture for pp elastic scattering. This construction is confirmed by other models, as illustrated in Fig.(11).
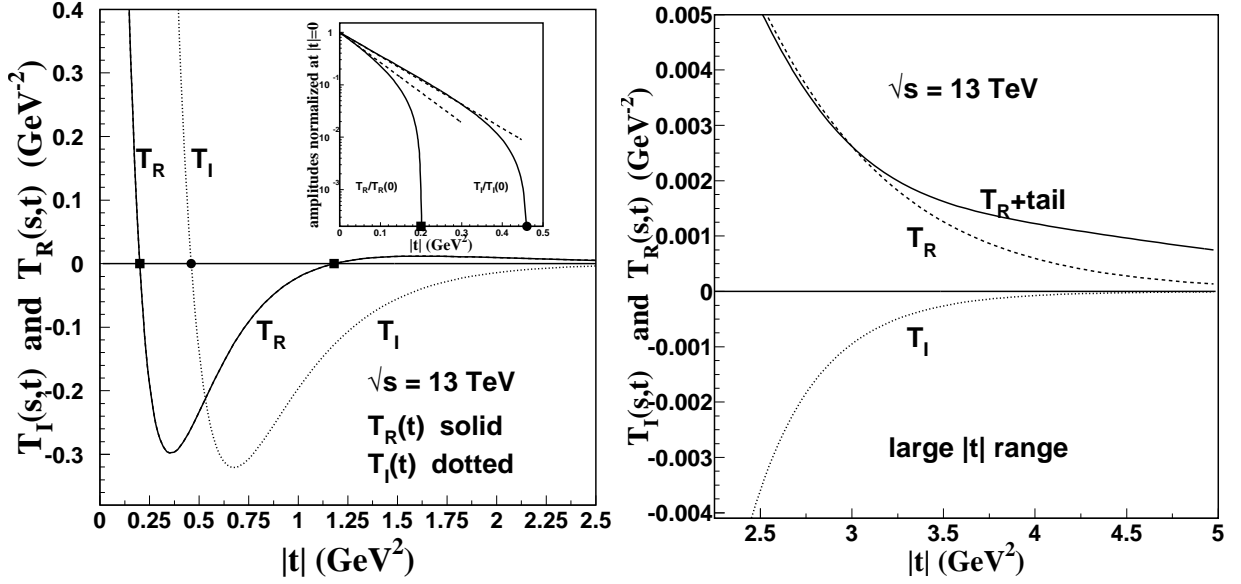
FIG. 6. $|t|$ dependence of the real and imaginary parts of the pp elastic amplitude at $\sqrt{s} = 13$ TeV, showing one zero at $Z_I = 0.46$ GeV$^2$ for $T_I(t)$, and zeros at $Z_R^{(1)} = 0.200$ GeV$^2$ and $Z_R^{(2)} = 1.180$ GeV$^2$ for $T_R(t)$. The inset uses log scale to exhibit the slopes at $|t| = 0$, demonstrating the early deviation of the amplitudes from the linear behaviour, each amplitude bending towards its zero. For large $|t|$ the negative imaginary amplitude (dotted line) becomes negligible, and there is strong dominance (in magnitude) by the positive real part (dashed line). For $|t|$ above $\sim 3$ GeV$^2$ the three-gluon exchange contribution added to the real part (solid line) raises $d\sigma/dt$, forcing the behaviour observed at $\sqrt{s} = 27.4$ GeV and conjectured to be universal. The continuity in the inclusion of the three-gluon exchange term is shown in Fig.5.
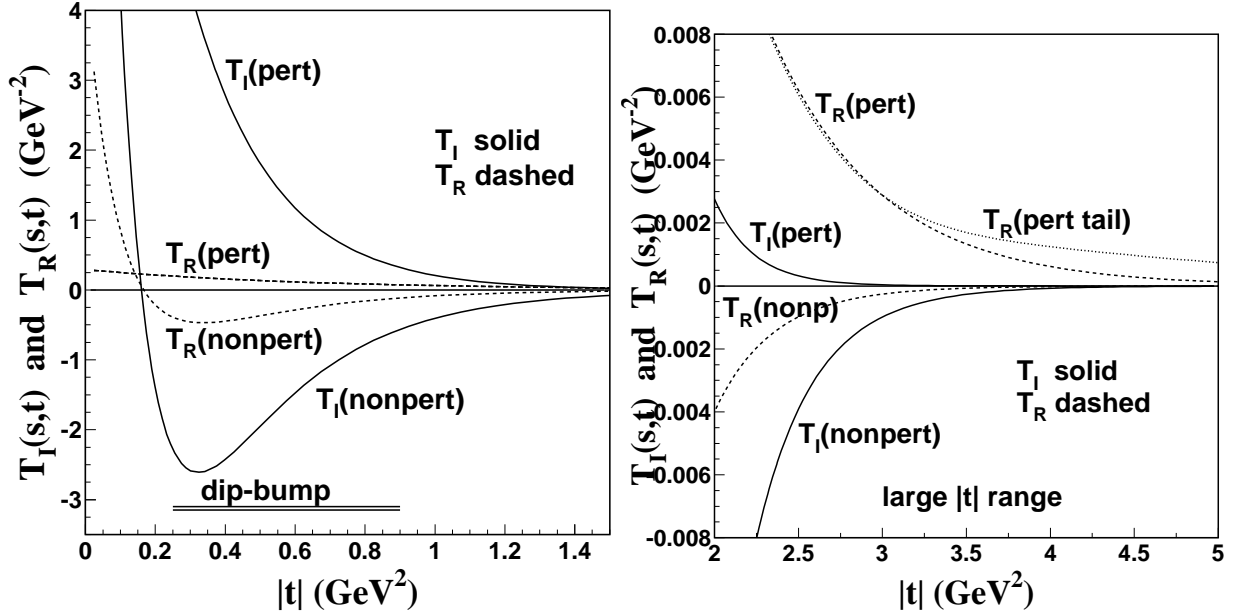


FIG. 7. Perturbative and non-perturbative contributions in $T_I(t)$ and $T_R(t)$. In the figure we call $T_K(\text{pert}) = \alpha_K e^{-\beta_K |t|}$, $T_K(\text{nonpert}) = \lambda_K \Psi_K(\gamma_K, t)$, (with $K = I, R$), and $T_R(\text{pert tail}) = T_R(\text{pert}) + R_{ggg}(t)$. It is important to observe that $\lambda_I/\alpha_I \approx 25/15$ and $\lambda_R/\alpha_R \approx 15$, so that the forward direction is dominated by the non-perturbative term, particularly so in the real amplitude (thus the evaluation of the $\rho$ parameter is mainly a non-perturbative affair). After the bump, $T_I(\text{pert})$ is negligible compared to $T_I(\text{nonpert})$, which becomes negligible compared to $T_R(\text{pert})$ for $|t| \geq 3$ GeV$^2$. For large $|t|$, only $T_R(\text{pert})$ (or $T_R(\text{pert tail})$ ) survives.

## B. Amplitudes in $b$-space

The $b$-space dimensionless amplitudes $\widetilde{T}_I(b)$ and $\widetilde{T}_R(b)$ of Eqs.(1,2) are shown in Fig.8a,b, where we observe that there are no zeros. In general $\widetilde{T}_I(b)$ is about 10 times larger than $\widetilde{T}_R(b)$, and it is impressive that the Fourier transforms of both have importance in the structure of the observed $d\sigma/dt$, with a dominance of the real part for large $|t|$. The function $\widetilde{T}_I(b)$ is monotonically decreasing in $b$, while $\widetilde{T}_R(b)$ has a maximum at $b = 4.339$ GeV$^{-1}$ with numerical value 0.131. At $b = 0$ we have

$$\widetilde{T}_I(b=0) = \alpha_I/2\beta_I = 1.81598 = \sqrt{\pi} + 0.04353$$

that is slightly larger than $\sqrt{\pi} = 1.7725$ and

$$\widetilde{T}_R(b=0) = \alpha_R/2\beta_R = 0.09487 .$$

At

$$b = b_{\rm root} = 1.47393\,{\rm GeV}^{-1}$$

we have

$$\widetilde{T}_I(b_{\rm root}) = \sqrt{\pi} = 1.7725 \quad {\rm and} \quad \widetilde{T}_R(b_{\rm root}) = 0.10009 .$$

As seen in Fig.8, the non-perturbative terms $\widetilde{T}_K(\text{nonpert}) = \lambda_K \widetilde{\psi}_K(b)$, $K = I, R$, dominate the amplitudes for large $b$, while $\widetilde{T}_I(\text{nonpert})$ dominates over $T_I(t)$ in the forward peak, where non-perturbative and perturbative magnitudes are in the ratio $\lambda_I/\alpha_I \sim 25/15$, with a ratio $\sim 25/9$ in the contributions to the total cross section. It is remarkable that forward elastic scattering is mainly a peripheral process of non-perturbative nature.

In terms of the $\widetilde{T}_K(s, \vec{b})$ amplitudes, the elastic, total and inelastic cross sections are written respectively

$$\sigma_{\rm el}(s) = \frac{(\hbar c)^2}{\pi} \int d^2\vec{b}\, |\widetilde{T}(s,\vec{b})|^2 \equiv \int d^2\vec{b}\, \frac{d\widetilde{\sigma}_{\rm el}(s,\vec{b})}{d^2\vec{b}} , \quad (21)$$

$$\sigma(s) = \frac{2}{\sqrt{\pi}}(\hbar c)^2 \int d^2\vec{b}\, \widetilde{T}_I(s,\vec{b}) \equiv \int d^2\vec{b}\, \frac{d\widetilde{\sigma}_{\rm tot}(s,\vec{b})}{d^2\vec{b}} , \quad (22)$$

and

$$\sigma_{\rm inel} = \sigma - \sigma_{\rm el} = (\hbar c)^2 \int d^2\vec{b}\, \left( \frac{2}{\sqrt{\pi}}\widetilde{T}_I(s,\vec{b}) - \frac{1}{\pi}|\widetilde{T}(s,\vec{b})|^2 \right)$$
$$\equiv \int d^2\vec{b}\, \frac{d\widetilde{\sigma}_{\rm inel}(s,\vec{b})}{d^2\vec{b}} . \quad (23)$$

The values of the integrated cross sections are $\sigma_{\rm el} = 31.096$ mb, $\sigma = 111.557$ mb, $\sigma_{\rm inel} = 80.461$ mb, with ratio $\sigma_{\rm el}/\sigma = 0.28$ . The differential cross sections in $b$-space shown in Fig.8c give a hint of the proton hadronic interaction structure in the transverse collision plane with smooth monotonous $b$-dependence.

Unitarity imposes that $\sigma_{\rm el} \leq \sigma$. With a classical point of view, a hypothesis that the inequality is valid for all $b$ is written

$$\widetilde{T}_I(s,\vec{b})^2 + \widetilde{T}_R(s,\vec{b})^2 \leq 2\sqrt{\pi}\, \widetilde{T}_I(s,\vec{b}) , \ \forall\, s, b \quad (24)$$

or

$$\widetilde{T}_R(s,\vec{b})^2 + (\widetilde{T}_I(s,\vec{b}) - \sqrt{\pi})^2 \leq \pi , \ \forall\, s, b . \quad (25)$$

This relation, called $b$-space unitarity, is satisfied by our amplitudes.

The eikonal function $\chi(s, b)$ for a given $s$ is introduced through

$$i\sqrt{\pi}\, (1 - e^{i\chi(b)}) \equiv \widetilde{T}(b) = \widetilde{T}_R(b) + i\widetilde{T}_I(b), \quad (26)$$

with

$$\chi(b) = \chi_R(b) + i\chi_I(b) . \quad (27)$$

Separating real and imaginary parts

$$1 - \cos\chi_R\, e^{-\chi_I} = \frac{1}{\sqrt{\pi}}\widetilde{T}_I(b) \quad (28)$$

and

$$\sin\chi_R\, e^{-\chi_I} = \frac{1}{\sqrt{\pi}}\widetilde{T}_R(b) \quad (29)$$

we obtain

$$\chi_I(b) = -\frac{1}{2} \log\left[ \frac{1}{\pi}\left( \widetilde{T}_R(b)^2 + (\widetilde{T}_I(b) - \sqrt{\pi})^2 \right) \right] . \quad (30)$$

so that the b-unitarity condition in Eq.(25) reads simply

$$\chi_I(s, b) \geq 0 \quad , \ \forall s, b. \quad (31)$$

With monotonic behavior of the scattering amplitudes, our solutions are restricted to the branch where $\chi_R \geq 0$. We need special care to write the expression for $\chi_R$, because it enters the second quadrant for small $b$. At the point $b = b_{\rm root}$ where $\widetilde{T}_I(b_{\rm root}) = \sqrt{\pi}$, $\cos\chi_R$ becomes zero, and it is negative between $b = 0$ and $b = b_{\rm root}$. To have continuity, avoiding that a calculator produces a positive value in the fourth quadrant, we must write the function arctan with two arguments. In the form used by the Wolfram Mathematica software, we write

$$\chi_R(b) = \arctan[(\sqrt{\pi} - \widetilde{T}_I(b)), \widetilde{T}_R(b)] \quad (32)$$
$$= \frac{\pi}{2} - \arctan[\widetilde{T}_R(b), \sqrt{\pi} - \widetilde{T}_I(b)] .$$

In terms of the eikonal function, we have

$$\frac{d\widetilde{\sigma}_{\rm el}(s,\vec{b})}{d^2\vec{b}} = 1 - 2\cos\chi_R\, e^{-\chi_I} + e^{-2\chi_I}, \quad (33)$$

$$\frac{d\widetilde{\sigma}(s,\vec{b})}{d^2\vec{b}} = 2\left( 1 - \cos\chi_R\, e^{-\chi_I} \right) , \quad (34)$$

$$\frac{d\widetilde{\sigma}_{\rm inel}(s,\vec{b})}{d^2\vec{b}} = 1 - e^{-2\chi_I} . \quad (35)$$

These expressions are plotted in Fig.8, and the explicit representation for $\cos \chi_R$ and the expression in Eq.(30) for $\chi_I(b)$ are plotted in Fig.9.

The function $\chi_I(b)$ is not monotonically decreasing, starting with $\chi(0) = 2.83208$ , and presenting a maximum at $b_{\max} = 1.2700$ GeV$^{-1}$ with value $\chi(b_{\max}) = 2.8818$. To detail this peculiar behaviour, and illustrate the effect of the real part, we point out that from Eqs. (28,29) we have

$$\chi_I(b) \leq -\frac{1}{2} \log\left(\frac{\widetilde{T}_R(b)^2}{\pi}\right) \equiv \text{bound}(b) . \qquad (36)$$

The expression bound$(b)$ is plotted in dotted line in Fig.9a. At $b = b_{\text{root}} = 1.47393$ GeV$^{-1}$, where $\widetilde{T}_I(b) - \sqrt{\pi} = 0$ , $\chi_I(b)$ touches bound$(b)$. Everywhere else, the inequality holds. This happens even at the maximum $b_{\max}$ of $\chi_I(b)$, where bound$(b_{\max}) = 2.8895$ is slightly larger than $\chi_I(b_{\max}) = 2.8818$.

It is interesting that the differential inelastic cross section $d\tilde{\sigma}_{\text{inel}}/d^2\vec{b}$ in Fig.8-c is almost fully saturated ($\simeq 1$) in the central collision region up to $b < 4$ GeV$^{-1} \approx 0.8$ fm. This can be seen also from the behavior of $\chi_I(b)$ in Fig.9, where for $b < 4$, it is $\chi_I > 1.5$ so that $\exp(-2\chi_I) \leq 0.05$. In the classical picture, from the central to approximately the half overlap impact parameter, the pp system behaves as completely absorptive, leading to particle production channels. We note, however, that this does not mean that the elastic differential cross section $d\tilde{\sigma}_{\text{el}}/d^2\vec{b}$ is null, due to the wave nature of the scattering. The diffractive wave as the reflection of inelastic scattering contributes to the elastic channel with almost the same magnitude as the inelastic one.

We also note that in the very peripheral collisions (say, $b > 9$ fm), mainly inelastic processes (small elastic contribution) are dominant. Physically speaking, this part can be associated to diffractive particle production mechanism. In $b$-space, this constitutes a slowly decreasing tail in $d\tilde{\sigma}_{\text{inel}}/d^2\vec{b}$. We may associate such processes (forward scattering) with those from the excitation of the vacuum through the non-perturbative processes. In [7] we argue that the existence of such a long tail in $d\tilde{\sigma}_{\text{inel}}/d^2\vec{b}$ and vanishingly small values of $d\tilde{\sigma}_{\text{el}}/d^2\vec{b}$ for large $b$, say $> 9$ fm, can be considered as responsible for the ratio, $\tilde{\sigma}_{\text{inel}}/\tilde{\sigma}$ being significantly larger than that of a black-disk limit, namely $1/2$. Assuming the geometric scaling property for $d\tilde{\sigma}_{\text{inel}}/d^2\vec{b}$, we extrapolated this ratio to 13 TeV, predicting the value

$$(\tilde{\sigma}_{\text{inel}}/\tilde{\sigma})_{\text{extrapolation}} = 0.7428,$$

while the present analysis gives

$$(\tilde{\sigma}_{\text{inel}}/\tilde{\sigma})_{\text{Totem}} = 0.7212,$$

which is 3% smaller, but yet definitely far from the black disk limit.
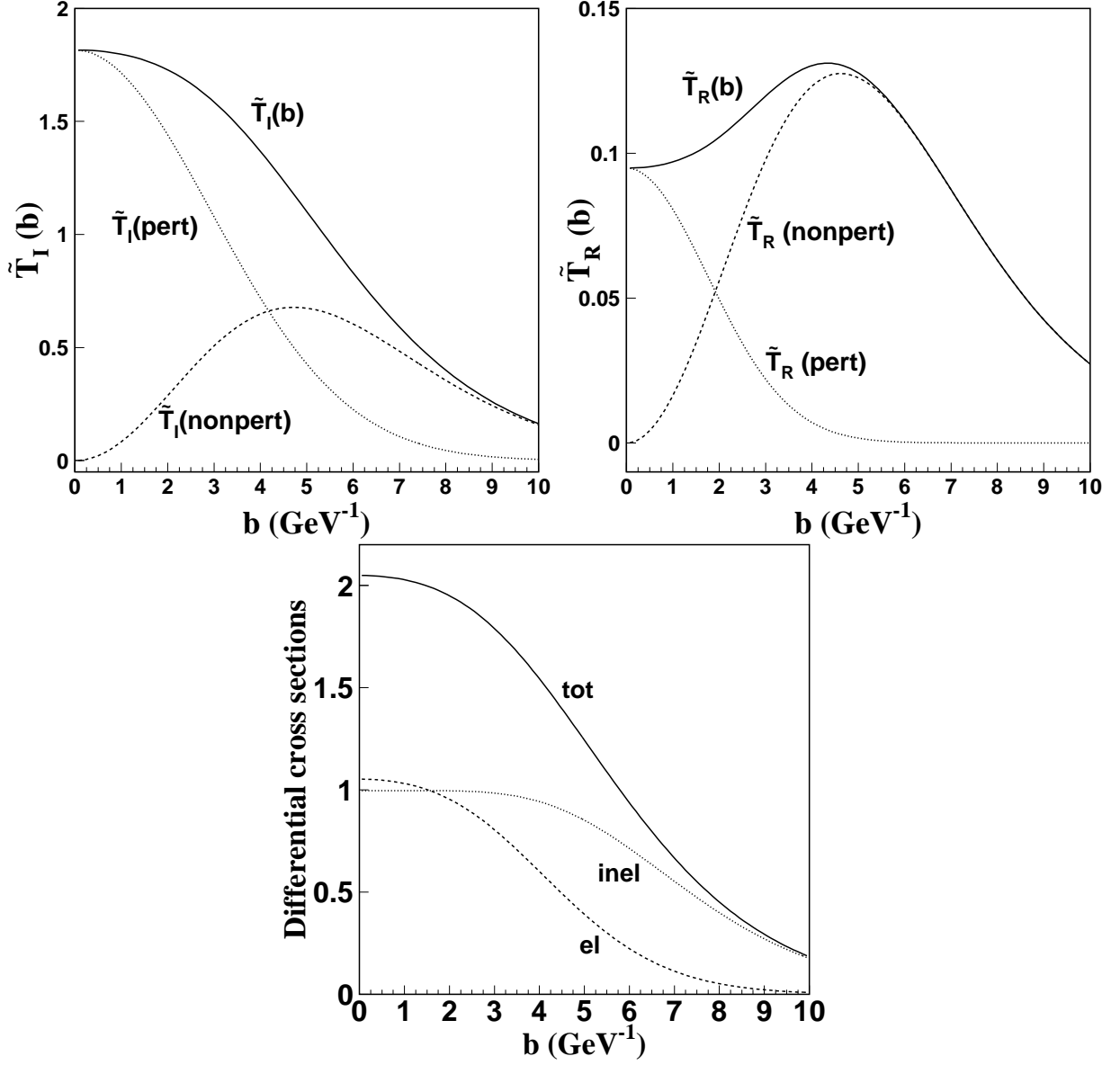
FIG. 8. a),b)- Amplitudes in b-space. The quantities labelled in the figures are $\widetilde{T}_K(\text{pert}) = (\alpha_K/2\beta_K)e^{-b^2/4\beta_K}$ , $\widetilde{T}_K(\text{nonpert}) = \lambda_K\widetilde{\psi}_K(b)$, with $\widetilde{\psi}_K(b)$ given in Eq.(2), and $\widetilde{T}_K = \widetilde{T}_K(\text{pert}) + \widetilde{T}_K(\text{nonpert})$. Notice the difference in the scales of the plots of $\widetilde{T}_I$ and $\widetilde{T}_R$. The perturbative terms dominate the central region of $b \leq 2$ GeV$^{-1} \sim 0.4$ fm while the non-perturbative terms are strongly dominating for large $b$. In c) the plots of differential cross sections of Eqs.(21,22,23) give hints about the structure of the interaction as observed in the transverse collision plane.
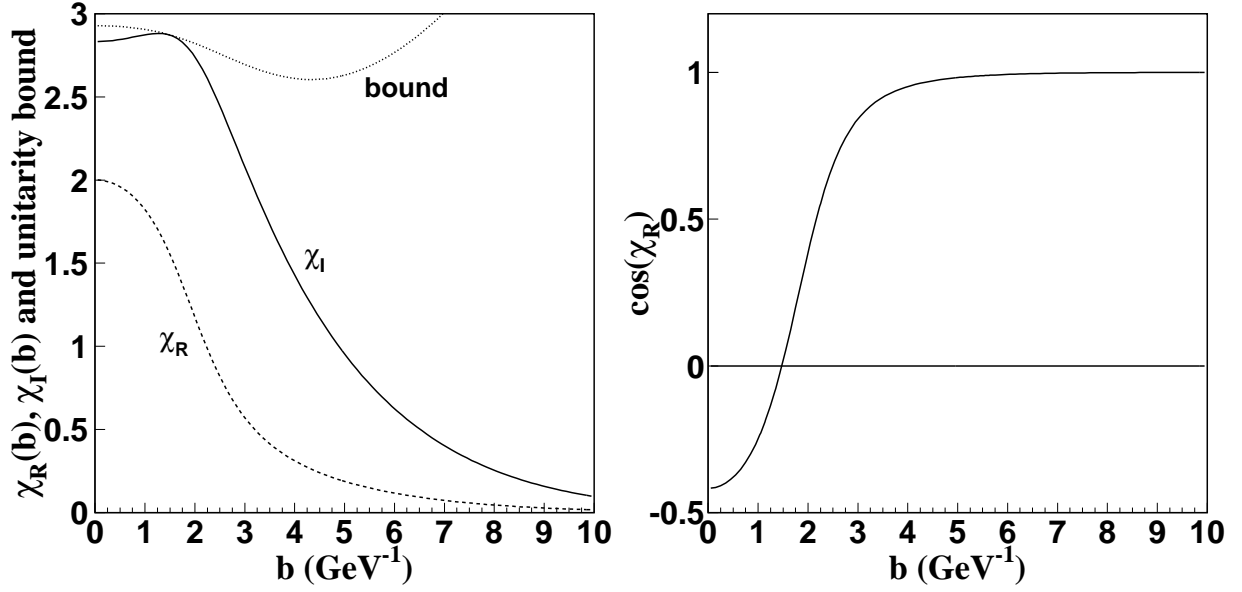
FIG. 9.    Eikonal quantities.  a) The quantity $\mathrm{bound}(b) = -(1/2)\log(T_R^2/\pi)$ shown with dotted line participates in the constraint of Eq.(36); b) $\chi_R(b)$ is in the second quadrant for small $b$ , with $\chi_R(0) = 2.0010$ , and $\cos\chi_R(0) = -0.4170$ ; at $b = b_{\mathrm{root}} = 1.4739$  GeV$^{-1}$, we have $\chi_R(b_{\mathrm{root}}) = \pi/2$ and $\cos\chi_R(b_{\mathrm{root}}) = 0$  .

## V. SVM AND OTHER MODELS

The present paper is dedicated to the analysis of the $|t|$ dependence of pp elastic scattering measured at 13 TeV. It does not deal with $s$ dependence, that was the purpose of previous work [7] and is treated by several authors [32]. The expressions of KFK model give high precision representation for the data with identification of the real and imaginary amplitudes, hopefully providing bridges between the observed quantities and fundamental dynamics. The quality of the description depends very sensitively on the parameter values, that are given in Table I. As the data points have values differing by several orders of magnitude, the reduction of decimal digits in the parameters may be disastrous.

Although consistent and complete, the significance of the results depends on the analytical forms used, and it is important to compare our predictions with the results obtained by other authors and in other frameworks. In this section we comment on some alternative formulations and models.

### A. Pomeron Models

Models based on Regge formalism are the most traditional in studies of hadronic scattering, giving connection for the $s$ and $t$ variables in observables of forward scattering for many hadronic systems. At high energies the dynamics is mainly formulated in terms of the exchange of one or two Pomerons and smaller contributions from Reggeons of non-zero spin and isospin. We here comment on some recent work [33–35].

The unique quality and extended $|t|$ coverage of the 13 TeV data deserves a specific quantitative investigation. The KFK amplitudes read the data to identify the parts of the complex amplitude. We believe that similar accuracy can be obtained with proper structure and fine tuning of parameters in the two-Pomeron contribution in the Regge model [33], with observation on the location of zeros, the position and height of the dip. The introduction of a term for connection with the three-gluon exchange amplitude may test the sign of the real part for large $|t|$.

The three-gluon contribution explains the difference in the dips of pp and p$\bar{\text{p}}$ scattering at 53 GeV [11, 12], where the magnitude at the dip is about $10^{-5}\text{mb}/\,\text{GeV}^2$ , while the magnitude of the dip at 13 TeV is 2000 times higher. For $\sqrt{s}$ in the TeV range [5] the three-gluon efect appears in the region of very large $|t| \geq 4$ GeV$^2$, not in the dip range.

The treatment of the $t$ dependence is not unique in Regge formalism. The contribution from two Pomerons is essential for the dip-bump structure in $d\sigma/dt$ and cannot be calculated without assumptions of form and of values of extra parameters [33, 34]. This term brings a negative sign that cancels the positive sign of the imaginary part of the single Pomeron term, and also contributes for the

formation of the second zero of the real part of the scattering amplitude. The calculations of the $|t|$ distribution of the 13 TeV data depend strongly on the fine tuning of parameters for the dip location, and do not seem to give good prediction for the value of the cross section at the dip, where we observe a deviation by a factor 2 [33]. We recall that our prediction [7] for location and height of the 13 TeV dip is confirmed as correct. Our feeling about the Regge model results [33] for the full $|t|$ distribution at 13 TeV, with $\chi^2$ values not given in the paper, is that the fitting is not precise. From the figures in the printed article we observe that the 1.8 and 7 TeV descriptions also are not precise.

The roles of the positive one-Pomeron (P) and the negative two-pomeron (PP) (and higher order terms) exchanges are similar to the roles of the first and second terms of the non-perturbative expression $\Psi(s,t)$ in KFK. The cancellation leads to the zero of the imaginary part, and consequently creates the dip. In the multi-Pomeron language, we would say that the KFK forms incorporate the P+PP+PPP ... series.

With $|t|$ dependence limited to the forward range, the analysis of the data [34] with Regge formalism uses energy dependence of the model to identify parameters of the amplitudes. Substantial changes in the parameters and in the expressions for the two-Pomeron exchange are introduced in relation to the paper of extended $|t|$ analysis [33]. Value of $\sigma$ is not given , and the results obtained for $\rho$ may be compared with the description specific for 13 TeV forward data accounting for the influence of the interference phase of the Coulomb and nuclear interactions [4].

A recent study of the energy dependence of $\sigma(s)$ and $\rho(s)$ includes the 13 TeV data in the statistical analysis of all data from $\sqrt{s} = 5$ GeV reported by the Particle Data Group (PDG), investigating the contributions of powers and/or logarithms in the Pomeron exchange terms [35]. The analytical form for $\rho(s)$ is given by dispersion relations, with one subtraction constant. The conclusion favors the choice of the parametrization with $\log s$ and $\log^2 s$ in $\sigma(s)$, excluding power forms. The parametrization leads to $\sigma(s) = 107.2$ mb, that disagrees with the treatments based on $d\sigma/dt$ measurements at 13 TeV, and leads to $\rho = 0.1185$ that agrees with KFK model for zero Coulomb interference phase. It is interesting to compare these results with the value $\rho = 0.135$ obtained also with Pomeron model [34] in a description of the energy dependence of forward scattering parameters. The effort shows the need of identification of terms and parameters for the phenomenology based on Regge formalism, using the new 13 TeV data for this clarification. The study does not include the $|t|$ variable or slopes, and obviously does not include Coulomb interaction.

The determination of the $|t| = 0$ parameters $\sigma(s)$ and $\rho(s)$ using the very irregular data basis of PDG is not secure, because the data basis supported by PDG has not been not submitted to a selection and evaluation of consistency and quality [36]. Values of $\sigma$ and $\rho$ are not

measured quantities, but rather are model dependent calculations, and in many cases the $d\sigma/dt$ measurements are not sufficient for a proper determination. On the other hand, at high energies of Fermilab and LHC, the reported values of $\sigma$ and $\rho$ have discrepancies that oblige alternative choices for statistical analysis. We thus find that the analysis of the data of $|t|$ distribution $d\sigma/dt$ at the single energy 13 TeV provides a more efficient and reliable method for determination of these quantities.

## B. Developments in SVM

The Stochastic Vacuum Model (SVM) is based on the functional integral approach to high energy scattering [14], with the physical motivation that soft hadronic reactions show manifestations of non-trivial QCD vacuum [15, 16]. The central element is the gauge invariant Wegner-Wilson loop, and physical quantities are obtained from the vacuum expectation values of the correlation of two loops. The correlation function is based on principles of gauge and Lorentz invariances, depending on internal coordinates of the loops and on their relative positions in the transverse collision plane, with parameters chosen according to lattice calculations. The gauge-invariant bilocal field strength correlation is integrated over minimal surfaces using the non-Abelian Stokes theorem, and calculated with a matrix cumulant expansion and a Gaussian approximation.

The amplitude in the eikonal approximation is factorized with product of the correlation of Wegner-Wilson loops (representing elastic scattering of two colour dipoles) and the factor with the dipole contents in the light-cone wave functions of the colliding hadrons. In simple effective form, the proton enters with a quark-diquark structure. After first calculations applying the stochastic vacuum model [13] to high energy scattering, improvements in the formal treatment of the tensor algebra turned more elegant the cumulant expansion [17].

Further developments of the application of SVM in hadron hadron scattering consisted in the combination of nonperturbative and perturbative (short range correlation) terms in the loop-loop correlation [18]. With this extension the model combines perturbative gluon exchanges with non-perturbative Stochastic Vacuum Model that has proved to lead to confinement of the color charges in the dipole via a string of color field [16]. This allows description of long and short distance correlations, in continuous transition that agrees with lattice results. The combination of perturbative and non-perturbative contributions was introduced before in phenomenology inspired in the model [11, 12].

In the perturbative correlation function an effective gluon mass is introduced to control the infrared range. This term enters in the overlap product with the proton dipole content to contribute to the profile function. KFK parametrizes the result obtained from the perturbative form through a simple Gaussian term in the profile

function as in Eq.(1).

Supported by lattice calculations [23], the correlation function can be assumed to have an exponential form, that is simpler than the general form used before [13]. The correlation length parameter of the correlation function establishes a length scale in the treatment of QCD vacuum properties, with value that enters in the precise calculations with KFK. SVM explores lattice results, considered as the main fundamental method to study QCD vacuum properties. Lattice calculations of correlation function are made in Euclidean space, and the necessary analytic continuation to Minkowski space [23] for the study of high energy scattering processes was developed [22] to formulate gauge-invariant dipole-dipole scattering.

The T-matrix element in SVM is purely imaginary, and with missing real part $d\sigma/dt$ cannot be calculated in the full $|t|$ range. The phenomenological representation in KFK introduces a real part that is a mirror image of the imaginary amplitude, and creates a tool to investigate the structure of the complex scattering amplitude in confrontation with data, possibly indicating directions of further progress in the theoretical foundations of SVM.

The dipole-dipole scattering amplitude has features of Pomeron exchange, describing only C=+1 charge conjugation. The model does not describe Odderon (C=-1) nor Reggeon exchange (quark-antiquark exchange), confortably since Pomeranchuk theorem says that C-odd effects disappear at high energies. The early predictions [18] for 14 TeV are $\sigma = 114.2$ mb and $B = 21.26$ GeV$^{-2}$.

## C. Martin's Formula for the Real Part

With basis on general principles of quantum field theory, A. Martin obtained a formula [37] connecting the real and imaginary parts of the complex amplitude of pp/p$\bar{\text{p}}$ elastic scattering. In principle the relation was established under restrictive conditions, as proximity of the asymptotic Froissart bound and limitation to the very forward range. The formula, that refers to the even component of crossing symmetry, includes also a scaling property incorporating energy dependence in the relation. The scaling property connecting $s$ and $t$ has been explored in several instances [38, 39], describing properties of the real and imaginary amplitudes in the forward range.

Without considering Martin's formula as a theorem with strict constraints, the relation can be considered as a suggestion for properties of the real part for the presently available high energies and applied for the full $|t|$ range in pp scattering. This extended view was adopted in the description of the data of Fermilab and ISR experiments in the range $\sqrt{s} =$19.4 - 62.5 GeV with effective success [40]. Both imaginary and real parts are fitted together, using a total of 12 parameters for each energy, with representations for real and imaginary parts connected by the formula. The numerical study includes also the 39

points of Faissler et al. measurements [8] at 27.4 GeV, considered as universally valid for the energy range investigated. In this study, the original Martin's real-part formula [37] was used without the full scaling property, namely it is applied separately for each energy investigated, with determination of the best parameters at each energy. The fittings of the ISR data show imaginary part with one zero and real parts with two zeros, just as we obtain in KFK model. In the very large |t| range the cross section receives contributions from both (positive) real and (negative)imaginary parts in the Formula, with dominant imaginary part.

The equation to be used is

$$T_R(s,t) = \frac{T_R(s,0)}{T_I(s,0)} \frac{d}{dt}\big[t\, T_I(s,t)\big] . \qquad (37)$$

Obviously $T_R(s,0)/T_I(s,0) = \rho$, but this quantity is not predicted by the formula, that specifically predicts the |t| dependence of the ratio $T_R(s,t)/T_R(s,0)$ once the imaginary part $T_I(s,t)$ is given.

We can reproduce this study with the 13 TeV data. Here we do not fit freely the imaginary and real parts, but rather take $T_I(t)$ as known and obtain a prediction for the real part by Martin's formula. That is, we write

$$\frac{T_R^{\mathrm{Martin}}(t)}{T_R^{\mathrm{Martin}}(0)} = \frac{d}{dt}\big[t\, \frac{T_I(t)}{T_I(0)}\big] . \qquad (38)$$

where $T_I(t)$ is the KFK proposal given in Sec.III. In Fig.10 we show KFK real amplitude normalized to one at the origin, namely we plot $T_R(|t|)/T_R(0)$ from KFK (solid line) and $T_R^{\mathrm{Martin}}(t)/T_R^{\mathrm{Martin}}(0)$ from Martin's formula in Eq.(38), with the given imaginary ratio $T_I(t)/T_I(0)$. The important point for the KFK model is the confirmation of the properties of the amplitudes: one zero for $T_I(s,t)$ and two zeros for $T_R(s,t)$. As in KFK, the real part is (now slightly) dominant over the imaginary part after the bump.

Although the prediction derived from Martin's Formula is to be considered in a qualitative level, the similarity of the real parts in KFK and in Martin's Formula is impressive. In a comparative plot of $d\sigma/dt$, the only remarkable difference is in the position and detailed shape of the dip-bump region.

### D. BSW and Selyugin (HEGS) models

The model proposed by Bourrely, Soffer and Wu (hereafter called BSW model) [41] gives explicitly the full s,t dependence of the elastic amplitudes and is appropriate for the comparison with our results. As shown if Fig.(11), the dip-bump structure occurs in similar |t| values, but there is a difference in $d\sigma/dt$ by a factor larger than 2 in this range. This difference results from the larger magnitudes (with negative signs) of both real and imaginary parts in the BSW model. In the RHS of the figure, the

plot is extended to very large |t| pointing out the connection with the supposedly universal tail at 27.4 GeV [8]. The broad dip in the region of 6 GeV² in the BSW calculation is due to a second zero in its imaginary amplitude, that is not included in the scale of the LHS.

The structure of the pp and p̄p interactions studied by O. Selyugin [42], based on the analysis of different sets of Parton Distribution Functions and introducing t-dependence in the Generalized Parton distributions, gives good representation of $d\sigma/dt$ data in large energy range, up to the LHC experiment at 13 TeV. We include in Fig.11 the |t| dependences of amplitudes in this model for 14 TeV.

The similarity of both BSW and Selyugin's with KFK calculations in the forms of the amplitudes is remarkable, reinforcing the expectation of the present work, that aims at a realistic disentanglement of the complex elastic amplitude.

### E. Other models

A work of purely statistical nature [43] reads the data at separate energies with about 10 parameters, without formal identification of the real and imaginary parts. The authors interpret that the approximately linear shape of $d\sigma/dt$ in the region after the bump is indication of a marked structure in the proton, as if there was a layer originating another peak in this region. In KFK this structure is determined by the smooth (in |t| ) real part, that is important and starts to become dominant in this region. The method deals statistically with all 13 TeV data (more than 400 points), and the behaviour of the six data points of large |t| is not influential, staying practically outside this analysis, as in other studies.

Similar conjecture of the existence of a layer-structure revealed in pp scattering at high energies is discussed by I.M. Dremin [44]. Again here, we claim that a proposal for the real and imaginary parts, with determination of their shapes, is essential for the investigation of the structure of the scattering process. The proposal that there are layers in the soup of quarks and gluon inside the proton because there is a range of nearly linear behaviour in $d\sigma/dt$, without identifying analytical forms for the amplitudes is not a well founded conjecture.

A paper [45] based on the Phillips-Barger model uses the formula for the complex amplitude [46]

$$A_{PB}(t) = i\big[\frac{1}{(1-t/t_0)^4}\sqrt{A}\mathrm{e}^{(Bt/2)} + \mathrm{e}^{i\phi}\sqrt{C}\mathrm{e}^{Dt/2}\big] \quad (39)$$

to parametrize $d\sigma/dt$ at several energies. With six free parameters, the 13 TeV data (398 points) are fitted with $\chi^2 = 6.30$ with statistical errors only. This value looks similar to our value 5.186 for 428 points in Table II. The

real part in the amplitude in Eq.(39) is a pure exponential form, without zero, very small in magnitude for all $|t|$, and with a value at the origin with $\rho = 0.02$. In the representative figure we observe that the fitting ignores the 10 points with $|t| \geq 2\,\text{GeV}^2$. Then we conclude that the representation is lucky in the value of $\chi^2$ but is unrealistic as a description of the physical data. The reference to odderon in the title is not meaningful, since the model is only a practical representation of pp cross section, and is not expected to predict behaviour of p$\bar{\text{p}}$ scattering.

## VI.    FINAL COMMENTS

Elastic scattering is described by one single complex function depending on two kinetic variables and it is natural to expect that investigations may lead to explicit and realistic (compatible with data and with any model independent information) expressions for both parts of this function. The present work presents explicitly real and imaginary amplitudes based on a QCD motivated model, and not just fits the observable $d\sigma/dt$. Besides, since the so-called impact parameter representation $(s, \vec{b})$ and its Fourier transform in $(s, \vec{q})$ space are both represented by simple analytical forms, we are able to observe unitarity and dispersion relation constraints, and discuss dynamical and geometric interpretations for the amplitudes.

The regularity in the energy dependence [7] adds reliability to our proposal. Characteristic features are the two zeros of the real part, and the single zero of the imaginary part, and this structure is reproduced by different models and frameworks. Since very precise representation of the data is obtained, the results suggest bridges between experiments and amplitudes that may serve as reference for microscopic dynamical models.

The interplay of the imaginary and real amplitudes at mid values of $|t|$ is responsible for the dip-bump structure of the differential cross section. We do not see indication for the existence of a structure with layers inside the proton. For large $|t|$ the perturbative term of the real part is dominant, while at small $|t|$ the imaginary nonperturbative term is stronger, occupying about 75 % of the cross section.

The amplitudes are treated as analytical forms valid for all $|t|$, describing all ranges with good accuracy. The deviation for a few points with large $|t|$ is common to other treatments, and doubt arises in the confidence on these points of the data, that have large error bars. In our treatment we fill the large $|t|$ with the connection to the range of three-gluon exchange, including 39 points of 27.4 GeV, producing $\chi 2 = 5.042$ (with statistical error bars only) for 467 data points.

The Yukawa-like behaviour for large $b$ of the profile function derived from the loop-loop interaction in the Stochastic Vacuum Model, that is incorporated in the input amplitudes in Eq. (2), is present in recent treatment of the pp interaction through Wilson loop correlation functions [23].

In KFK model the parameters of the real and imaginary parts of the elastic amplitude are treated independently. Strictly speaking, this procedure may not guarantee that the final amplitude is analytic when $s$ and $t$ are extended to the complex domain. This concern would impose further constraints, particularly in extrapolation to higher energies. The qualitative agreement of the real part in KFK with the prediction from Martin's Real Part Formula shown in Fig.10 is very important. The questions of analiticity and crossing symmetry, with explicit inclusion of energy dependence, as in frameworks exploring scaling properties [39], require further study.

## VII.    ACKNOWLEDGEMENTS
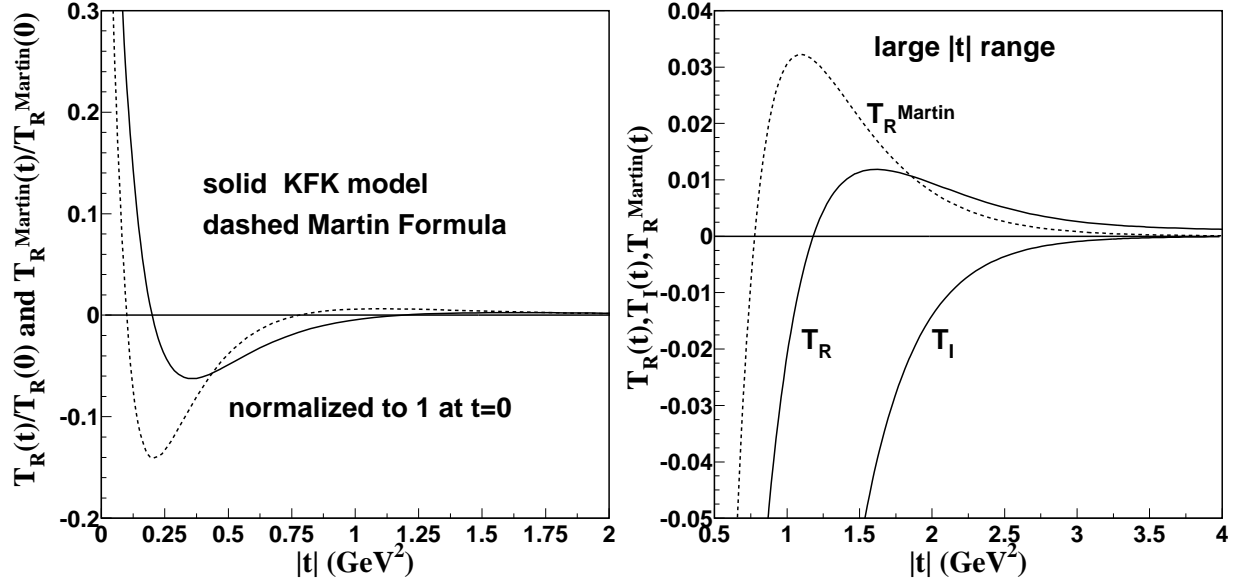
FIG. 10. Martin's Real Part Formula. a) $|t|0$ dependence of the real part of elastic amplitude calculated with Martin's Formula $T_R^{\mathrm{Martin}}(t)$ using the imaginary part $T_I(t)$ of KFK model, compared with $T_R(t)$, both normalized to 1 at $|t| = 0$; b)large $|t|$ behaviour of $T_R(|t|)$ and $T_I(|t|)$ of KFK calculation compared with the prediction $T_R^{(}Martin)$ from Martin's Formula using same $T_I(|t|)$. The real amplitudes are both positive and dominant (slightly in the case of Martin's Formula) over the negative imaginary part.
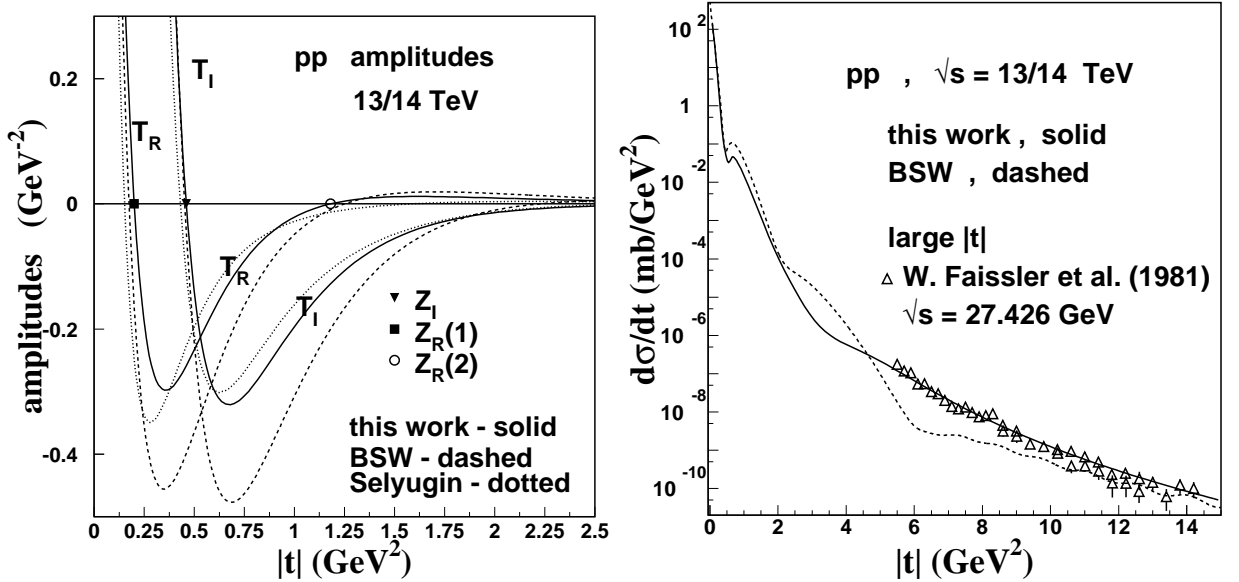


FIG. 11. Scattering amplitudes $T_R(t)$ and $T_I(t)$ in comparison with other models. In a) (LHS) our solution of Eqs.(11,14) and Table I in solid line; BSW model [41] in dashed line ; Selyugin model [42] in dotted line. The solutions are similar, with one zero in $T_I(t)$ and two zeros in $T_R(t)$ with impressive coincidence of positions, and with dominance of the real part (with positive sign) for large $|t|$. In b) (RHS) Calculation of the BSW model [41] (dotted line) covering the large $|t|$ range of 27.4 GeV measurements [8], compared with solution of KFK model including $R_{ggg}(t)$. The prediction of the BSW model is not precise in the dip-bump region, but the inclusion of the tail for large $|t|$ is very interesting.

[1] G. Antchev et al. , Totem Coll. , Eur.Phys.J. C79 (2019) no.9, 785.

[2] G. Antchev et al. , Totem Coll., Eur.Phys.J. C79 (2019) no.10, 861.

[3] G. Antchev et al. , Totem Coll. , Eur.Phys.J. C79 (2019) no.2, 103.

[4] A.K.Kohara, E. Ferreira and M. Rangel , Phys. Lett. B789, 1-6 (2019).

[5] A. K. Kohara, E. Ferreira, T. Kodama, *Phys. Rev. D* **87**, 054024 (2013).

[6] A. K. Kohara, E. Ferreira, T. Kodama, *Eur. Phys. J. C* **73**, 2326 (2013).

[7] A. K. Kohara, E. Ferreira, T. Kodama, *Eur. Phys. J. C* **74**, 3175 (2014).

[8] W. Faissler et al., Phys. Rev. **D 23**, 33 (1981).

[9] S. Conetti et al., Phys. Rev. Lett. **41**, 924 (1978).

[10] A. Donnachie and P. V. Landshoff, *Zeit. Phys. C* **2**, 55 (1979); *Phys. Lett. B* **387**, 637 (1996).

[11] E. Ferreira and F. Pereira, *Phys. Rev. D* **59** , 014008 (1998).

[12] E. Ferreira and F. Pereira, *Phys. Rev. D* **61**, 077507 (2000).

[13] H.G. Dosch, E. Ferreira, A. Kramer *Phys. Rev. D* **50**, 1992 (1994).

[14] O. Nachtmann, Ann. Phys. **209**,436 (1991).

[15] H.G. Dosch, Phys. Lett. B **190**, 177 (1987)

[16] H.G. Dosch and Yu.A. Simonov, Phys. Lett. B **205**,339 (1988)

[17] E.R. Berger and O. Nachtmann, *Eur. Phys. J. C* **7**, 459 (1999).

[18] A.I. Shoshi, F.D. Steffen and H.J. Pirner, Nucl. Phys. A **709**, 131 (2002).

[19] A. Di Giacomo and H. Panagopoulos, Phys. Lett. B**285**,133 (1992) .

[20] H.G. Dosch and E. Ferreira, Eur. Phys. Journal **C29** , 45-58 (2003).

[21] H.G. Dosch and E. Ferreira, Eur. Phys. Jour. **C52**, 83-101 (2007).

[22] A.I. Shoshi, F.D. Steffen, H.G. Dosch and H.J. Pirner, Phys. Rev. D **68**, 074004 (2003).

[23] M. Giordano, E. Meggiolaro and N. Moretti , JHEP **09**, 031 (2012).

[24] A. Martin, *Phys. Lett. B* **404**, 137 (1997).

[25] A. Afanasev, P.G. Blunden, D. Hasell, B.A. Raue, Prog. Part. Nucl. Phys. 95, 245-278 (2017).

[26] M. Guidal, M.V. Polyakov, A.V. Radyusikin, M. Vanderhaeghen, Phys. Rev. **D72**, 054013 (2005).

[27] A. Breakstone et al, Phys. Rev. Lett. **54**, 2180(1985).

[28] C. Ewerz, https://arxiv.org/abs/hep-ph/0306137.

[29] Y.V. Kovchegov and E. Levin, " Quantum Chromodynamics at High Energy " , (Cambridge University Press, Cambridge, England, 2012);

[30] E. Nagy et al., Nucl. Phys. B **150**, 221 (1979).

[31] N. Amos et al., Nucl. Phys. B **262**, 689 (1985).

[32] R. Fiore, L. Jenkowszki, R. Orava, E. Predazzi, A. Produkin and O. Selyugin, Int. J. Mod. Physics **A 24**, 2551 (2009).

[33] A. Donnachie and P. V. Landshoff, *Phys. Lett. B* **727**, 637 (2013) .

[34] A. Donnachie and P. V. Landshoff, *Phys. Lett. B* **798**, 135008 (2019) .

[35] M. Broilo, E.G.S. Luna and M.J. Menon, *Phys. Rev. D* **98**, 074006 (2018).

[36] E. Ferreira, A.K. Kohara and J. Sesma, *Phys. Rev. D* **98**, 094029 (2018).

[37] A. Martin, *Lett. Nuovo Cim.* **7**, 811 (1973).

[38] J, Dias de Deus, Nucl. Phys. B **59**,231 (1973).

[39] A.K. Kohara, J. Phys. G **46**,12, 125001 (2019).

[40] D.A. Fagundes and M.J. Menon , *Int. J. Mod. Physics A* **26**, 3219 (2011).

[41] C. Bourrely, J.M. Myers, J.Soffer and T.T. Wu , *Phys. Rev.D* **85**, 096009 (2012).

[42] O.V. Selyugin, *Eur. Phys. J. C*(2012), 72:2073 ; talk presented at Diffraction 2014 ; private communication is gratefully acknowledged.

[43] T. Csörgo, R. Pasechnik and A. Ster , Eur. Phys. J. C **79** :62 (2019).

[44] I. M. Dremin, Eur. Phys. J.C **80**, 172 (2020).

[45] V.P. Gonçalves and P.V.R.G. Silva, Eur. Phys. J. C **79**, 237 (2019).

[46] D. Fagundes et al., Phys. Rev. D **91**, 114011 (2015).